Key Points:

- Eruption of a coronal mass ejection (CME) from an active region on the solar limb may be able cause major terrestrial space weather disturbance
- Comparison of recent events observed using modern equipment gives key insights on great historic events such as the role of substorms
- The longitudes at which low-latitude aurora is seen depends on the Universal Time of the CME impact on Earth's magnetosphere

Author Contributions:
Conceptualization: Mike Lockwood, Dechen Gyeltshen
Formal analysis: Mike Lockwood, Mat J. Owens, Luke A. Barnard, William Brown, Dechen Gyeltshen
Funding acquisition: Mat J. Owens
Investigation: Mike Lockwood, Mat J. Owens
Methodology: Mike Lockwood, Luke A. Barnard, William Brown
Project administration: Mike Lockwood
Resources: Mat J. Owens
Software: Mike Lockwood, Luke A. Barnard, William Brown
Supervision: Mat J. Owens
Validation: Mat J. Owens, Luke A. Barnard, Dechen Gyeltshen
Visualization: Mike Lockwood
Writing – original draft: Mike Lockwood
Writing – review & editing: Mat J. Owens, Luke A. Barnard, William Brown, Dechen Gyeltshen

Can a Major Geomagnetic and Auroral Disturbance Originate From a Solar Active Region Close to the Limb?

Mike Lockwood[1] , **Mat J. Owens[1]** , **Luke A. Barnard[1]** , **William Brown[2]** , and **Dechen Gyeltshen[1]**

[1]University of Reading, Reading, UK, [2]British Geological Survey, The Lyell Centre, Edinburgh, UK

Abstract When forecasting major geomagnetic storms, it is commonly assumed that coronal eruptions near the solar limb are not of concern. We here discuss two sequences of events: the Fátima storms of January 1938 and the Halloween storms of October/November 2003. In both cases, a highly active sunspot group generated a major eruption when it reached the western solar limb. In the 2003 events, this generated no terrestrial disturbance, despite being estimated to be the most powerful flare on record. In contrast, the only known solar eruption that could have given the second Fátima storm, was the major flare on the western limb. The geomagnetic aa_H and Dcx indices in this storm exceeded disturbance levels that have been seen for less than, respectively, 0.0015% and 0.0091% of the time and caused aurora to be seen at geomagnetic latitudes down to 26.5° (at Tataouine, Tunisia), making it the 13th most extensive auroral event known since the Maunder minimum. We investigate if this storm was caused by the limb eruption and conclude that it would be a possible but rare occurrence, although the historic data do not allow us to fully eliminate other scenarios. We show that the longitude distribution of low-latitude auroral sightings depends upon the Universal Time of the impact of the coronal mass ejection and the subsequent timing of substorm activity is consistent with the theory of how low-latitude red aurora is generated. We show how the Dcx and aa_H indices give understanding of the substorm behavior during historic events.

Plain Language Summary Coronal Mass Ejections launched from active regions close to the edge of the solar disc are usually assumed to miss the Earth and so not cause a major disturbance to terrestrial space weather. We discuss an event in January 1938 which may be an example that shows that this is not always the case. Conversely, we discuss a similar event in 2003 which caused no effect at Earth, despite the associated limb flare being estimated to be the most powerful on record. We also use these events to demonstrate that the longitudes on Earth where low-latitude aurora are seen depend on the Universal Time of the impact of the coronal mass ejection on the Earth, which has implications for our understanding of how such aurora is generated.

1. Introduction

Coronal Mass Ejections (CMEs) launched close to the solar limb are usually assumed to miss the Earth and so not cause a major disturbance to terrestrial space weather. Many authors have found that only a small percentage of CMEs released from near the limb caused a geomagnetic disturbance, and these were mainly only modest storms (Cid et al., 2012; Gopalswamy, Mäkelä, et al., 2009; Gopalswamy, Yashiro, et al., 2009; Gopalswamy et al., 2010; Kim et al., 2005; Rodriguez et al., 2009; Zhang et al., 2007). From results such as these, it has become a widely-accepted paradigm for space-weather forecasting that limb events do not cause major storms. In this paper we study a historic event, the second Fátima storm in January 1938, which appears to have arisen from a sunspot group very close to the limb yet generated a storm that caused a major auroral event. Lockwood et al. (2025) have recently shown that in terms of low-latitude auroral extent, this storm is the 13th largest known, with aurora extending down to magnetic latitudes that have been reached on only 0.01% of nights since 1650. We here show this storm also caused a maximum ring current disturbance that has been exceeded on only 0.01% of the time in the 92 years between 1932 and July 2024 (the interval covered by the ring current index used) and a mid-latitude geomagnetic disturbance level that has only been exceeded for 0.0015% of that interval. Observers at the time noted how unusual it was that a sunspot group so close to the solar limb gave rise to such a large geomagnetic storm (Anonymous, 1938; Nicholson, 1938) and subsequent authors have discussed this exceptional event (Hayakawa et al., 2021; Lefèvre et al., 2016; Newton, 1943). We here look at two possible hypotheses: (a) This large event was caused by a CME launched by the large active region close to the limb, implying the CME had an

unusually large heliographic longitudinal extent (Carcaboso et al., 2024; Lugaz et al., 2008; Magdalenić et al., 2014) and/or was subject to non-radial propagation with azimuthal (longitudinal) defelection towards Earth (Gopalswamy, Mäkelä, et al., 2009; Gosling et al., 1987; Kahler et al., 2012; Kay et al., 2017; Mäkelä et al., 2013; Mohamed et al., 2012; Temmer et al., 2014) or (b) the CME was launched at close to the same time as the large limb flare by an unusually small active region closer to the center of the solar disk or was an unusually geo-effective "stealth" CME that did not originate from an active region (He et al., 2018; Mishra & Srivastava, 2019; Nitta & Mulligan, 2017; Nitta et al., 2021; Yardley et al., 2021). The paucity of data makes it hard to distinguish these two possibilities, but either makes the event highly unusual.

The Fátima storms have been described in detail by Hayakawa et al. (2021). We here compare with the Halloween storms of October/November 2003 (Hady, 2009; Villante & Regi, 2008; Wu et al., 2005) which are similar in many ways, and in particular, the causal active region generates a massive flare very shortly after it had rotated off the Eastern limb of the Sun: in the case of sunspot group responsible for the Halloween storm the flare is estimated to be the largest flare ever recorded (Brodrick et al., 2005). However, unlike the second Fátima storm, the CME associated with this flare missed the Earth and did not cause a geomagnetic disturbance.

By comparison with the Halloween storms, we make deductions about the substorm activity during the Fátima storms. We investigate the likely substorm behavior during the Fátima storm. Magnetic storms, such as the Fátima events, are large-scale, long-duration disturbances in Earth's coupled magnetosphere-ionosphere-thermosphere system that last between several hours and a few days. In this paper we detect them using an index compiled from low latitude magnetometer data that largely responds to increased global ring current intensity during storms. Substorms, in contrast, are more localized, short-duration (1–3 hr) disturbances that involve rapid energy release from the magnetotail, causing auroral brightening and enhanced currents in the ionosphere (the Auroral Electrojet [AE]) (e.g., Pulkkinen, 2007). Substorms occur frequently during storms and they do inject energetic particles that enhance the ring current. Hence substorms used to be thought of as quantum elements of storms. However, we now know that substorms are not the primary cause of the ring current enhancements which, instead, are predominantly caused by enhanced convection in the magnetosphere (Daglis et al., 1999; Ebihara & Ejiri, 2003; Schulz & Lanzerotti, 1974; Wygant et al., 1998). However, understanding of the ionospheric signature of magnetospheric convection shows that the substorm cycle is the response to enhanced magneto-spheric convection (Cowley & Lockwood, 1992; Lockwood & Cowley, 1992, 2022) and so injection of particles into the ring current during storms and substorms are intimately linked, even though the particles are, in the main, not directly injected by the substorm. This link opens up the possibility of using historic geomagnetic data on the ring current to infer substorm behavior. In this paper storms are identified using the *Dcx* geomagnetic index and substorms using the *SML* geomagnetic index, which are both described later in this paper.

Another facet of major storms is that the aurora extends to unusually low geomagnetic latitudes. These low-latitude aurora are usually predominantly red in color (Mikhalev, 2024), indicating low energy precipitating electrons. They last for several hours and usually occur when a sequence of magnetospheric substorms is in progress during a storm (Miyaoka et al., 1990; Rassoul et al., 1992; Shiokawa et al., 1994; Tinsley et al., 1986). Later, during the recovery phase of the storm, monochromatic red-line Stable Auroral Red (SAR) arcs form at these lower latitudes (Kozyra et al., 1997). SAR arcs are thought to be generated by downward heat conduction carried by low-energy (<10 *eV*) electron precipitation that is produced when high energy ring-current particles interact with the low-energy denser plasma in the plasmasphere. The red auroras seen during the main phase of the storm appear to be caused by a somewhat similar mechanism to SAR arcs, but their onsets are because of a very large storm-time increase in ring current ion fluxes which interact with the low energy plasma in the plasmasphere in the midnight sector (Shiokawa et al., 2013). This being the case, the migration of these red aurora to very low-latitudes during storms occurs because of the Earthward intrusion of the ring current around midnight (Kataoka et al., 2024), as seen in Energetic Neutral Atom imaging of the ring current during storms (Shiokawa et al., 2013).

2. The Fátima Storms

Figure 1 presents a summary of the Fátima storms in January 1938. Panel a shows the Quasi-Dipole geomagnetic latitudes of "area-combined auroral samples" of auroral observations, Λ_M.

Lockwood et al. (2025) confirm the result from prior studies that these QD geomagnetic coordinates (or the similar Apex coordinates) are optimum for ordering auroral phenomena. Magnetic Apex coordinates are calculated by tracing along magnetic field lines of the magnetic field model from the point in question, *P*, to the
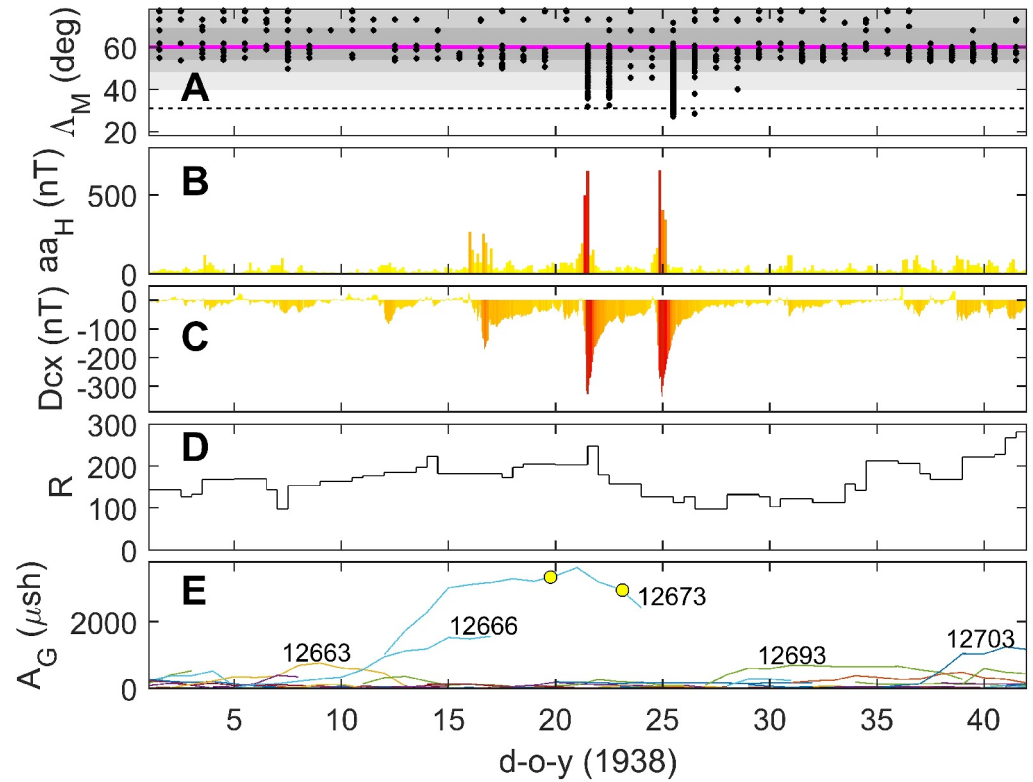
Figure 1. Summary of the Fátima storms in January 1938. (a) The quasi-dipole geomagnetic latitude of area-combined auroral observations, Λ_M, as used in the survey by Lockwood et al. (2025). The light-gray, mid-gray, and darker-gray areas delineate Λ_M values that are within, respectively, the $\pm 3\sigma$, $\pm 2\sigma$, and $\pm 1\sigma$ points of the distribution for all area-combined samples in the survey, which covers January 1650 to July 2024. The mean of that distribution is shown by the mauve line. The horizontal dashed line is the -4σ point of the distribution ($\Lambda_M = 31°$) and was used by Lockwood et al. (2025) to define 21 extreme events since the Maunder minimum, in which aurora was observed equatorward of this threshold: the second Fátima storm is ranked 13 in that list. Panel (b) shows the 3-hourly values of the homogeneous aa geomagnetic activity index, aa_H, in a bar-chart format, where the vertical bars are colored according to their height. Panel (c) is the same as (b), but for hourly values of the Dcx geomagnetic index. (d) The International sunspot number R. (e) The area (in millionths of a solar hemisphere, μsh) of sunspot groups visible on the solar disk: the yellow dots mark white-light solar flares that occurred in the dominant group, 12673. Note that the horizontal axis is in fractional day-of-year (d-o-y), which is zero at 00:00 *UT* at the start of 1 January 1938.

highest point above the Earth (the apex) allowing for the deformation of the Earth's surface from a spherical form. In this paper we only need the International Geomagnetic Reference Field, IGRF (Alken et al., 2021), which can be used for all times after 1900. If the field line apex is at a geodetic height, h_a and the point in question is at a geodetic height h. The Modified Apex (MA) latitude, Λ_A, is defined relative to a constant reference height h_r by

$$\Lambda_A = \pm \cos^{-1}\left(\frac{R_E + h_r}{R_E + h_a}\right)^{1/2} \tag{1}$$

where R_E is the mean radius of the Earth. The sign is positive in the Northern magnetic hemisphere and negative for the Southern. The quasi-dipole (QD) latitude is very similar to Λ_A but is defined relative to the geodetic height of the point P, h_p.

$$\Lambda_M = \pm \cos^{-1}\left(\frac{R_E + h_p}{R_E + h_a}\right)^{1/2} \tag{2}$$

Hence MA and QD latitudes are very similar; however, MA latitudes do not depend on the height of the point P (being referred to a constant altitude, h_r). For $h_r = h_p$ the two are the same but diverge if $h_r > h_p$. QD coordinates are useful for phenomena with a specific height profile because they allow for h_p and do not depend on a defined

reference height. Reviews of MA and QD coordinates have been given by Richmond (1995) and Laundal and Richmond (2017). Lockwood et al. (2025) show maps of them for various epochs and compare them with other coordinate systems and with particle precipitation data.

The area-combined samples measure was devised by Lockwood et al. (2025) to reduce the effect of concentrations of potential observers in major centers of population and also to remove duplication of reports of a single observation in different catalogs: reports of aurora from locations that are separated by less then 0.2° in great-circle distance are treated as a single area-combined sample and the QD geomagnetic latitude computed for the central location (the means of the geographic latitudes and longitudes of the reports that are combined). The light-gray, mid-gray and darker-gray areas in Figure 1a delineate Λ_M values that are within, respectively, the $\pm 3\sigma$, $\pm 2\sigma$, and $\pm 1\sigma$ points of the distribution for all area-combined samples in the survey by Lockwood et al. (2025), which covers January 1650 to July 2024. The mean of that distribution is shown by the mauve line. Panel (b) shows the 3-hourly values of the homogeneous *aa* geomagnetic activity index, aa_H (Lockwood, Chambodut, et al., 2018; Lockwood, Finch, et al., 2018) in a bar-chart format, where the vertical bars are colored according to their height. The aa_H index is based on the same data as the *aa* index (Mayaud, 1972) but accounts for the secular drifts in the magnetic latitudes of the stations and inter-calibrates stations in one hemisphere by regressing the data from their overlap periods as a function of both time-of-year and time-of-day. This generates hemispheric series which are in much closer agreement than the corresponding hemispheric indices of *aa* and gives good agreement with other long geomagnetic data series (Lockwood et al., 2022). The aa_H index series used here covers 156.6 years from the start of 1868 to July 2024. Panel (c) of Figure 1 is the same as (b) for hourly values of the *Dcx* geomagnetic index, which we use in preference to *Dst*. *Dcx* was introduced by Karinen (2005) and has a number of advantages: *Dcx* extends back to 1932, giving us 92 full years of data, whereas *Dst* only extends back to 1957 and hence, unlike *Dcx* does not include the Fátima storms of 1938. *Dcx* is also more homogeneous in its construction and uses more stations with better weightings than *Dst* (Mursula et al., 2011). Like *Dst*, *Dcx* is increasingly negative for greater disturbance levels and is strongly modulated by the ring current in Earth's inner magnetosphere. (However, both are also influenced, to a lesser extent, by the currents that flow in the magnetopause boundary). In hourly means, the *Dst* and *Dcx* indices are not that well correlated (linear corelation coefficient 0.544 for the interval 1956–2024, inclusive) because *Dcx* gives onset and peak times of storms that can be more than an hour different in time from those for *Dst* due to the fact it uses more stations and so records those times with greater accuracy. For daily means from the same interval the correlation rises to 0.763 and the best linear regression is given by the equation

$$Dcx = 0.674.Dst - 1.270 \tag{3}$$

where both *Dst* and *Dcx* are in *nT*. Hence, for approximate comparisons, *Dcx* is about 70% of *Dst*. The root-mean-square fit residual using Equation 3 for daily means is 11.1*nT* in *Dcx* and 16.4*nT* in *Dst*.

Parts (d) and (e) of Figure 1 show solar data. Part (d) shows the international sunspot number, *R*: it can be seen that *R* was close to 200 before the first Fátima event (from the distribution of *R* over the 1868–2024 interval of the aa_H data, this level is exceeded 9.1% of the time) but thereafter fell to about 100 after the second event (a level exceeded 34.7% of that time). Panel (e) shows the area of the sunspot groups (in units of millionths of a solar hemisphere, *μsh*). This is dominated by sunspot group number 12673 in which two white light flares were detected by observers at the Royal Greenwich Observatory (RGO) at the times marked by the yellow dots (Jones, 1955; Nicholson, 1938). The first of the flares was observed at 18:20 *UT* on 20 January 1938 (day-of-year, d-o-y, 19 in Figure 1 which defines d-o-y as zero at 00:00 *UT* at the start of 1 January). Note that Corrected Universal Time (*UTC*) was introduced in 1960, using atomic-based standard for timekeeping - hence for the Fátima events we refer to the old standard (*UT*) but for the Halloween storms of 2003, and others after 1960, we refer to its modern equivalent, *UTC*. The second flare occurred at 02:54 *UT* on 24 January. The flares precede the two geomagnetic and auroral storms (on 22 January and 24/25 January) by similar lags and, as no other flares were detected and there were no other large sunspot groups present, these flares appear to be associated with the launch of the Coronal Mass ejections (CMEs) that we infer hit the magnetosphere, generating the two storms. However, later in this paper we will investigate other potential sources.

Figure 2 studies the Fátima storms of January 1938 in greater detail. Part a shows the variation in *Dcx*. For both storms, the start of the positive phase, indicating the onset of the magnetospheric compression, is marked by a
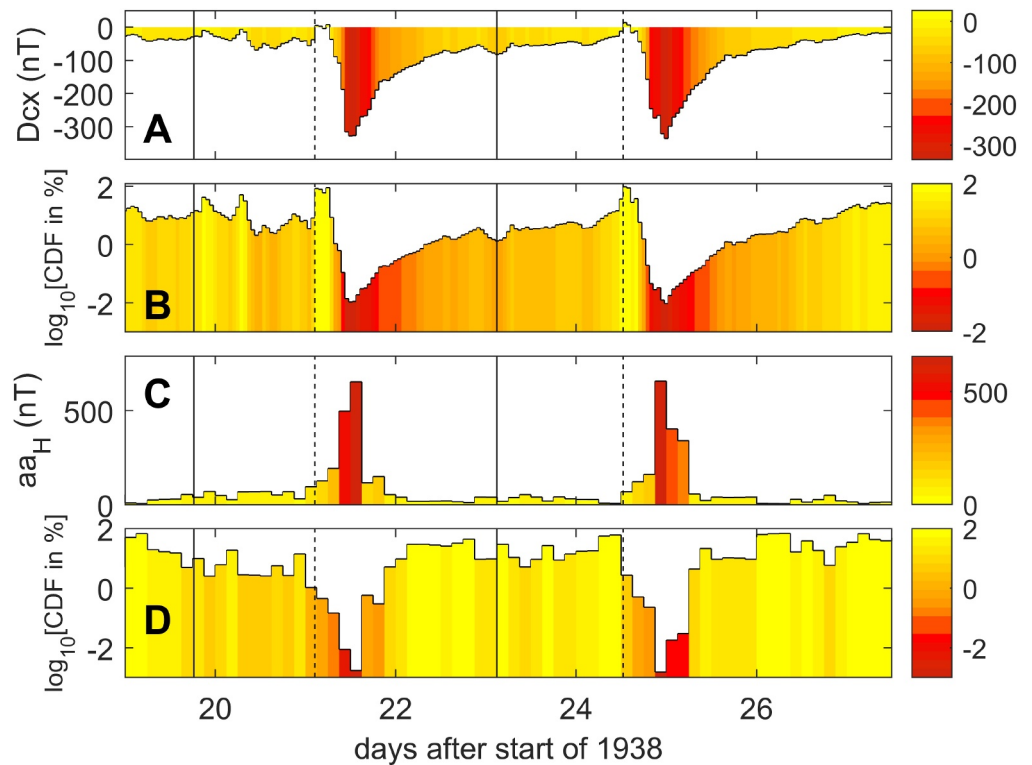
Figure 2. Detail of the variations of (a) the Dcx index and (c) the aa_H index during the two Fátima storms. Parts (b) and (d) show the variations in Cumulative Distribution Function (expressed as a percentage and on a logarithmic scale) for the values shown in (a) and (c). In both cases, the percentage the distribution of all values (from the interval 1932–2024.5) than the value at that time is plotted so (b) plots the log of the percentage of Dcx values lower (i.e., more disturbed) than the value at that time, whereas (d) plots the percentage of aa_H values that are greater (i.e., again more disturbed) than the value at that time. Note that a (logarithmic) scale value of 2 corresponds to 100% and −2 corresponds to 0.01% and the color scales are arranged so that red/yellow corresponds to a higher/lower geomagnetic disturbance level. The vertical solid lines mark the times of the peaks of the flares and the vertical dashed lines mark the Coronal Mass Ejection arrival at Earth, causing the onset of the short positive phase in Dcx as the dayside magnetosphere is compressed. Note also that the horizontal axis is, as in Figure 1, zero at 00 UT on 1 January 1938 and so the flares that peaked at 18:20 UT on 20 January and 02:54 UT on 24 January appear at 19.76 dy and 23.12 dy, respectively, on this axis.

vertical dashed line. The vertical solid lines show the times of the peaks of the observed white-light flares. Panel (b) shows the percentage of all the Dcx values that are lower (greater activity) than the values shown in Part (a).

The first Fátima storm starts at 02:30 UT on 22 January after the flare which peaked at close to 18:20 UT on 20 January, giving a propagation lag from flare to magnetopause impact of $t_L = 32.2$ hrs. At this time, the sun-Earth distance, d was equal to 0.984 $AU = 1.472 \times 10^8$ km, giving an average transit velocity from the peak of the flare to Earth of $v = d/t_L = 1225$ kms^{-1}. The start of negative phase of the Dcx storm was 4 hrs later and the minimum of negative phase was at 11:30 UT on 22 January, 5 hrs after the start of the negative phase. The storm at the $Dcx < 150$ nT level lasted 14 hrs and at the $Dcx < 250$ nT level lasted 8 hrs. In aa_H, the storm at greater than the 250 nT level lasted 6 hrs, between 09:00 UT to 15:00 UT. The minimum Dcx was −326.4 nT, an activity level that is exceeded just 0.011% of the time in the full 92-year Dcx data set. Note that many auroral sightings during this event were recorded as being on 21 January, even though impact on Earth magnetosphere was in the early hours of 22 January. This is because many observers (knowingly or not) use an astronomical definition of an observing "night" that extends past local midnight.

The peak of the flare ahead of the second Fátima storm was at 02:54 UT on 24 January. Impact on Earth (again defined by the onset of the positive phase of the storm in Dcx) was at 12:30 UT on 25 January. Hence, if that flare was the source of the storm the propagation time is $t_L = 33.6$ hrs, yielding an average transit velocity from flare to Earth of $v = d/t_L = 1217$ kms^{-1}. The positive phase of Dcx again lasted 4 hrs and the minimum of the negative phase was 7 hrs later. At the $Dcx < -150$ nT and $Dcx < -250$ nT levels, this storm lasted 16 hrs and
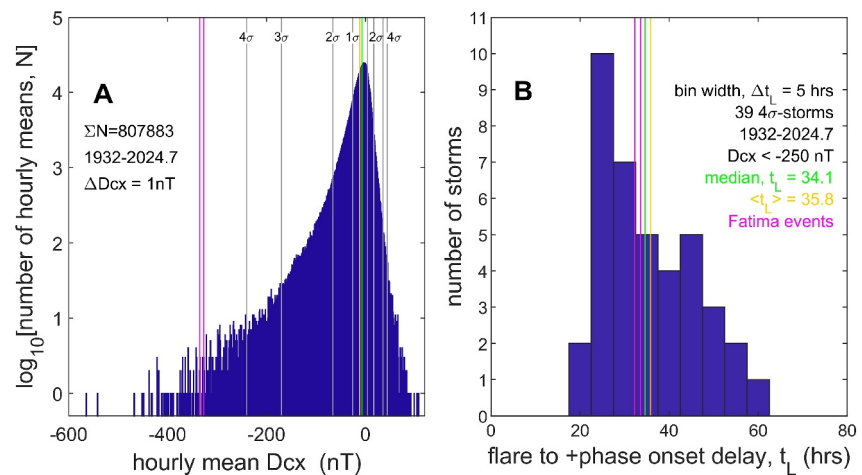
**Figure 3.** (a) The distribution of the 807,883 hourly Dcx index samples available between 1932.0 and 2024.7. The numbers of samples in bins that are $\Delta Dcx = 1 \, nT$ wide are plotted on a logarithmic scale. The gray lines give the 1σ to 4σ values for the two tails of the distribution, and the mean and median are shown by the orange and green lines, respectively. The two mauve lines are the peak disturbances (minimum Dcx) of the two Fátima events of 1938. (b) The distribution of the lags t_L between the peak of the associated solar flare and the subsequent onset of the positive phase of the Dcx disturbance, for the 39 isolated 4σ storms (for which Dcx falls below $-250 \, nT$). Only isolated storms for which the associated flare can be identified are included. The green, orange and mauve lines are, respectively, the median, the mean, and the Fátima events values (assuming that the second Fátima storm was associated with the observed white light flare).

11 hrs, respectively. In aa_H the 250 nT level was exceeded for 9 hrs. The minimum Dcx was $-335.8 \, nT$ an activity level that is exceeded 0.0095% of the time in the full Dcx data set.

Hence, the two storms were very similar from a terrestrial perspective. Storm 2 is sightly stronger in geomagnetic indices and lasts a little longer. The estimated average transit velocity from the flare to the magnetopause was marginally lower for the first storm. Hence the flare seen in white light ahead of the second Fátima storm was very close to the time that we expect the causal eruption to have happened on the Sun.

Figures 3 and 4 place the Fátima events in context. Figure 3a shows the distribution of hourly Dcx values for the 807,883 hourly values available between 1932.6 and 2024.7. The largest storm in the Dcx data, ranked by the minimum Dcx reached, is that on 13/14 March 1989, this is the event that caused a 9-hr outage of Hydro-Québec's electricity transmission system. In this event, Dcx fell to $-564.5 \, nT$ and aa_H rose to 722.3 nT, a level that is exceeded by just two hourly samples in the interval of the Dcx data (1932–2024.5), that is, 0.0009%, and by just four 3-hourly samples in the interval of the aa_H data (1868–2024.5), that is, 0.0007%. Figure 3a shows that both the Fátima storms are larger than the 4σ level of the distribution of all Dcx values (which is $-250 \, nT$).

Figure 3b plots the distribution of the lags between the associated flare and the onset of the subsequent magnetopause compression, t_L, for the 39 isolated storms in the Dcx data set during which Dcx falls below the 4σ level of $-250 \, nT$. These delays have been derived in the same way as was used for the Fátima storms. This means that the timing of the arrival at Earth's magnetosphere is taken to be the onset of the positive phase of the storm in all cases. Identification of the associated flare is not always straightforward, and events with multiple onsets—for which associating of the relevant flare is ambiguous—have been omitted. Of course, this is a major difference between historic storms and more recent ones, as we now have an ability to track the causal CME from its solar source to the Earth and have X-ray and EUV observations of flares which makes them easier to detect than in white light, particularly for events near the center of the solar disk. We here do not use such information on specific cases so that the treatment of events is homogeneous. However, we can apply knowledge gained from recent studies to devise the rules of selection. Studies predict that the energies available to eject CMEs limits their velocity to 3000 kms^{-1} (Gopalswamy et al., 2005) and, if this velocity were not reduced by drag in traversing the interplanetary medium, this would give a limit to t_L of about 14 hrs. An exceedingly fast CME passed over the STEREO-A spacecraft at a heliocentric distance of 1 AU on 23 July 2012 at a speed of 2930 kms^{-1}, just slower than the predicted limit for ejection of such events. It is thought that the interplanetary drag in this case was reduced by a series of prior events that cleared the way for the CME. The reconstructed flare flux peaked at 02:42
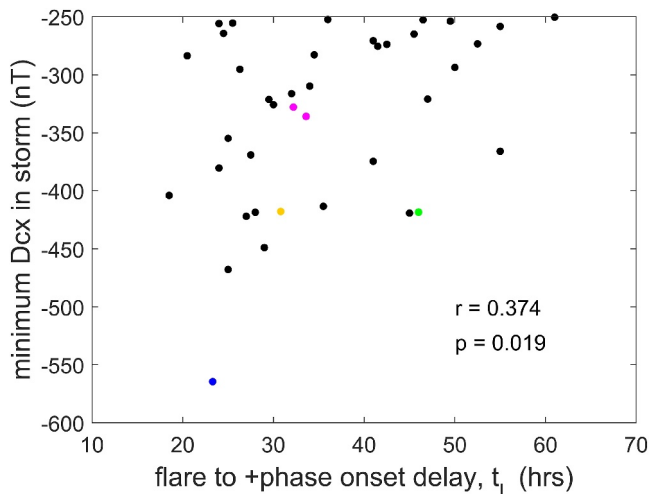
Figure 4. Scatter plot for the 39 isolated storms from 1932 to 2024.5 which reach Dcx below $-250\ nT$ (used to compile the distribution shown in Figure 3b). The minimum Dcx in the storm is plotted as a function of the flare-to-magnetosphere lag, t_L. The linear correlation coefficient is $r = 0.374$ which gives a p-value of the null hypothesis that there is no relationship of $p = 1.9\%$. The mauve points are the two Fátima storms, the blue point the 13/14 March 1989 storm, the orange point is the 10/11 May 2024 storm and the green point the last of the "Halloween" series of storms on 20 November 2003.

UT on 23 July and the CME shock reached STEREO-A at 23:52 UTC on the same day: this gives a flare-to-1AU lag of $t_L = 21.2$ hrs (Liu et al., 2014). This is a very fast CME, but still has a larger t_L the value of 18 hrs inferred for the Carrington event (Muller, 1990). However, even this may not be the fastest CME. The event on 4 August 1972 yields a value of $t_L = 14.2$ hrs (Knipp et al., 2018), marginally greater than the theoretical minimum. This event is not included in our survey as the response in Dcx shows a double feature (so it is not isolated) and because the minimum Dcx reached was only $-139\ nT$. However, this event was fast enough to generate exceedingly high fluxes of Solar Energetic Particles, so great they would have posed great risk to Apollo astronauts (Lockwood & Hapgood, 2007), and there were a variety of unusual space weather effects (Knipp et al., 2018). Hence, we here discount flares for which t_L would be less than the theoretical minimum estimate of 14 hrs. In all cases, we use the flare peak identified in previous studies of geomagnetic storms by Newton (1943), Cliver and Crooker (1993), or Lefèvre et al. (2016). In general these agree, but not in all cases: in the few cases where these papers disagree, the flare identified by Lefèvre et al. (2016) is used here.

Figure 3b shows that the Fátima storms have t_L values that are just slightly lower than the mean and median of the distribution for these $Dcx < -250\ nT$ events. Figure 4 looks at the relationship between the t_L value and the peak magnitude (minimum Dcx) of these 39 storms. The mauve dots are the Fátima storms, the blue point the 13/14 March 1989 storm (the lowest Dcx in the full 1932–2024.6 Dcx data set), the orange point is the 10/11 May 2024 storm studied by Hayakawa et al. (2025) and Lockwood et al. (2025) and the green point the last of the "Halloween" series of storms on 20 November 2003, which is discussed later in the present paper. The plot shows there is a weak correlation such that shorter lag times tend to give greater storms; however, there is much scatter in the data (linear correlation coefficient $r = 0.374$). That correlation is, nevertheless, quite significant with only as 1.9% chance that it arose by chance. Hence, low transit times are associated with geoeffective CMEs but there other key factors, chief among which is the dimension of the event in the direction of motion, which sets the duration of the traversal over Earth (Owens et al., 2025), and the variation in the orientation of the interplanetary magnetic field which controls the extraction of solar wind and CME energy by the magnetosphere. Note also that Figure 4 only surveys large geomagnetic storms (minimum Dcx below $-250\ nT$) and it is possible that there are smaller storms with low t_L values.

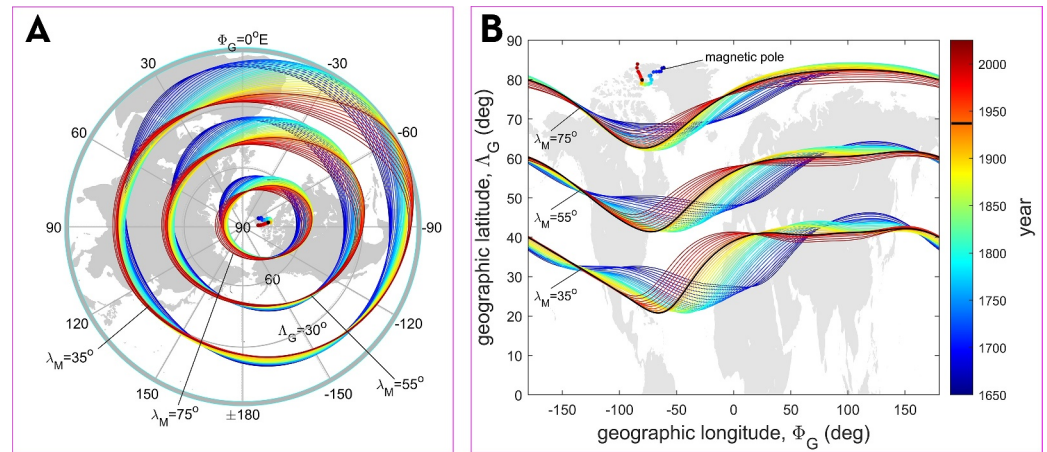## 3. Aurora During the Fátima Storms

As discussed by Lockwood et al. (2025), Quasi-Dipole (QD) coordinates are good geomagnetic coordinates to use when studying aurora. The geographical distribution of QD coordinates has varied with the secular variation of the intrinsic main field of Earth, symptoms of which are the (different) motions of the geomagnetic poles in the two hemispheres.

Figure 5 shows polar and Mercator maps of northern-hemisphere—contours of three Λ_M values (35°, 55° and 75°) for dates 10 years apart between 1655 and 2025, which in each of the three cases are colored from blue for 1650 to dark red for 2025. The dots of the same color show the locations of the North Pole at these dates. The black lines are for 1938 it can be seen the motion of the pole is associated with significant changes in Λ_M at some longitudes (particularly over Europe, North Africa and the Atlantic Ocean) but very little change at other longitudes (particularly over the Western USA and the Pacific Ocean).

Figure 6 shows maps of locations where aurora were observed. Part a shows the locations of all "area-combined samples" for January 1650 to July 2024. As described by Lockwood et al. (2025), a total of 223,916 reports on 136,966 nights were combined into 195,233 independent area-combined samples by averaging the locations that were less than 0.2° apart in great-circle distance. This separation was chosen from considering how close observers need to be to see (at an elevation 30° above the horizon) the same auroral form, which is at a typical green-line altitude of 110 km. This prevents undue weighting being given to sightings of the same auroral form over a

Figure 5. (a) Polar and (b) Mercator maps (in geographic latitude Λ_G and longitude ϕ_G coordinates) of contours of constant Quasi-Dipole geomagnetic latitude, Λ_M for years 10 years apart between 1655 (in blue) and 2025 (in deep red). The contour relevant to the Fátima events is for 1938, which is shown in black and sits on the orange to red border of the color scheme. The geomagnetic North Pole locations ($\Lambda_M = 90°$) are given by the correspondingly colored dots. Three sets of contours are shown in each part, for Λ_M of 35°, 55° and 75°.
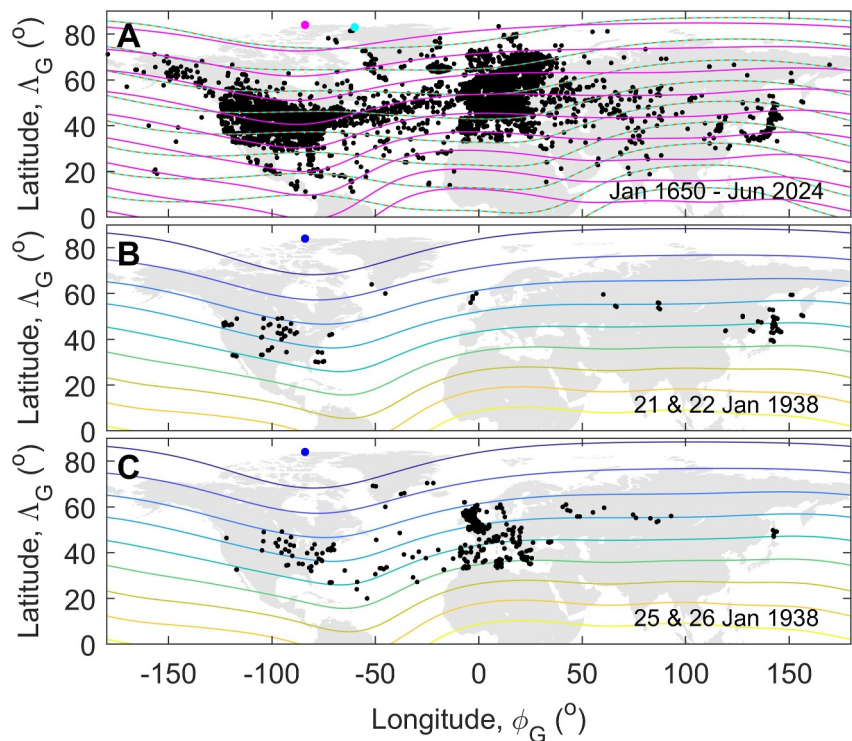
Figure 6. The Northern-Hemisphere distribution of area-combined auroral observations ("samples") used in this paper. Part (a) is for all the 191,660 area-combined samples from the interval January 1650 to July 2024. The mauve contours are quasi-dipole (QD) geomagnetic latitudes, Λ_M, of [**0**:10°:80°] for 2024 and the brown and cyan dashed contours are the same for 1650. The mauve and cyan dots give the corresponding north magnetic pole locations for these years. Part (b) is for the 120 samples on the nights of 21 and 22 January 1938. The colored contours (yellow to dark blue) are QD geomagnetic latitudes, Λ_M, of [**0**:10°:80°] for 1938 and the blue dot is the north magnetic pole location. Panel (c) is the same as (b) for the 454 samples on the nights of 25 and 26 January 1938.
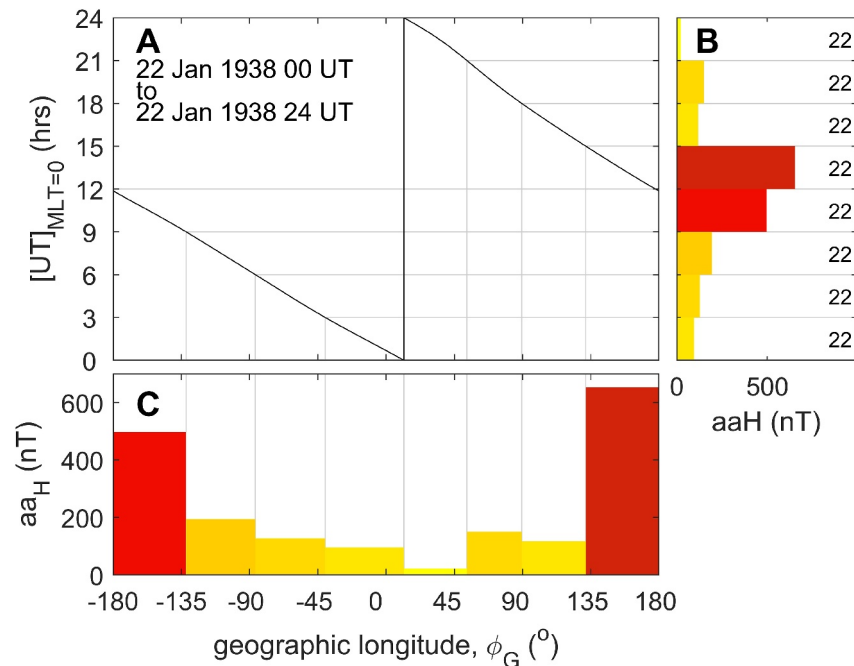
Figure 7. Analysis of the effect of Universal Time (UT) on the first Fátima storm on 22 January 1938. Part (a) shows the variation with geographic longitude (positive East), ϕ_G, of the UT at which the Magnetic Local Time is 0 hr (magnetic midnight) along the contour of Quasi-Dipole magnetic latitude of $\Lambda_M = 31°$. Part (b) shows the value of the 3-hourly aa_H index (horizontal axis) as a function of UT. The bars in (b) are labeled by the day number in January 1938 (in this case all 22). Using panel (a) this is mapped onto a variation with ϕ_G shown in (c).

place of high population density. This also removes many duplications of the same report which arise when it is copied from one catalog into another. Lockwood et al. (2025) show that at middle and low latitudes, auroral report numbers, as one would expect, correlate with population density. The Southern Hemisphere is 80.9% covered by water whereas the same figure for the Northern Hemisphere is 60.7% and currently 87% of Earth's population is in the Northern Hemisphere (U.N., 2024) and this percentage was slightly greater still in 1938 (Frederico, 2023). Hence, the number of potential observers is much greater in the Northern than the Southern Hemisphere and they are also more evenly spread in longitude. In addition, historically, the number of auroral reports were was much slower to grow in the Southern Hemisphere. Hence, we restrict our survey to Northern Hemisphere data only. The contours show the lines of constant Λ_M for values between zero and 80° in steps of 10°: the mauve lines are for 2024, the end of the interval, and the brown and cyan dashed contours are the same for 1650, the start of the interval.

Parts (b) and (c) show the locations where aurora was observed during the first and second Fátima storms, respectively. A major difference is immediately apparent with the event of 20/21 January 1938 giving reports centered on Pacific longitudes (with observations being predominantly in the Far East or the western USA) whereas the event of 24/24 January 1938 gave reports centered on Atlantic longitudes with reports mainly from Europe and the eastern USA (and a significant number from trade ships crossing the Atlantic between the two). The colored contours are again for Λ_M of [**0**:10°:80°] for the year 1938.

During geomagnetic storms, red aurora is seen at low geomagnetic latitudes, Λ_M. These displays last for several hours and usually occur when a sequence of magnetospheric substorms is in progress during a storm (Miyaoka et al., 1990; Rassoul et al., 1992; Shiokawa et al., 1994; Tinsley et al., 1986). The presence of substorms would also raise the mid-latitude range index aa_H. In Figures 7 and 8 we map the UT of the storm peaks in the aa_H index onto geographic longitudes using the UT at which the Quasi-Dipole (QD) geomagnetic latitude of $\Lambda_M = 31°$ is at 0 hr (midnight) in Magnetic Local Time (MLT). This QD latitude was adopted by Lockwood et al. (2025) as a threshold for an extreme event and is very close to the 4σ point of the distribution of all area-combined auroral samples over the interval 1650–2024.5. The MLT is calculated from the magnetic longitude in QD coordinates using Equations 14 and 92 of Laundal and Richmond (2017).
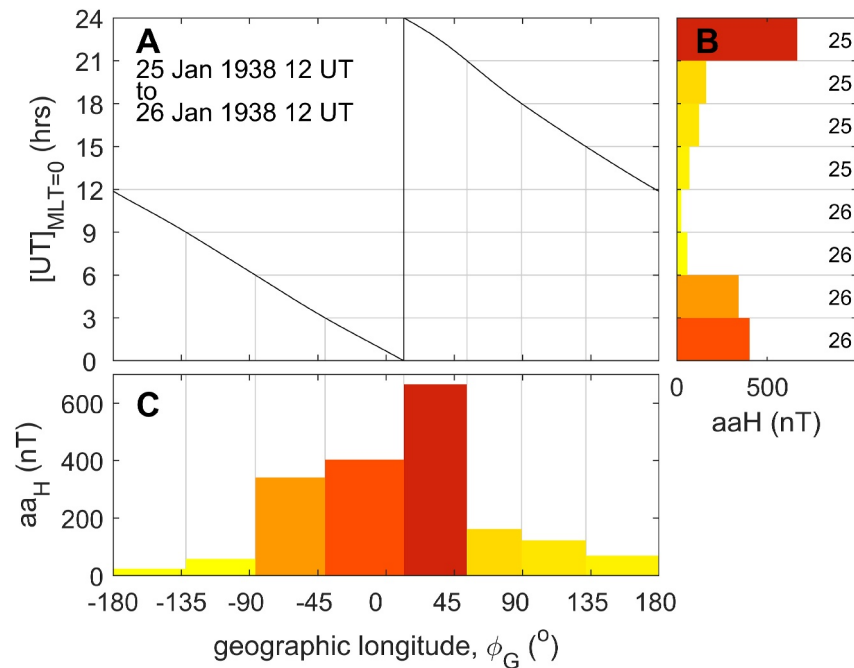
Figure 8. The same as Figure 7 for the second Fátima storm on 25/26 January 1938. Note that the Universal Time variation starts at 12 *UT* on 25 January and ends at 12 *UT* on 26 January and the bars in (b) are labeled by the day number in January (25 or 26).

Figures 7 and 8 explain the different longitudinal structure of auroral sightings during these two storms, as seen in Figure 6. As discussed above, our database of auroral sightings is from the Northern Hemisphere only, but we note that Hayakawa et al. (2021) show soundings from both hemispheres and find many sightings in Australia and New Zealand (but none in South Africa or South America) during Fátima storm 1 which fits with the longitudinal distribution seen in the Northern Hemisphere in Figure 6b. In contrast, for Fátima storm 2 Hayakawa et al. (2021) find only 4 sightings in the Southern Hemisphere. The sightings in Figure 6 are somewhat more spread than predicted from aa_H in Figures 7 and 8 but it should be remembered the mapping uses only MLT of 00 hr whereas typically low-latitude aurora in the Northern Hemisphere is seen over an extended range of MLT around midnight, typically 20 hrs to 02 hrs (Grandin et al., 2024).

Lockwood (2023) has shown that, statistically, considerably greater solar wind forcing (in terms of integrated estimated magnetopause reconnection voltage), Φ_D is needed to drive a substorm at around 15 *UTC* than at 2 *UTC*. Lockwood (2023) also found evidence for this using a global MHD model of the magnetosphere that indicates that this is associated with the hinge bending of the geomagnetic tail between the near-Earth tail (oriented by the geomagnetic field) and the mid/far tail (oriented by the solar wind). This being the case, this factor will influence all storms. Therefore, the *UT* of arrival of storm 2 means it would have needed larger Φ_D to drive a substorm than did storm 1.

4. Sunspot Groups During the Fátima Storms

Figure 9 shows reconstructions of the major features seen on the solar disk ahead of the Fátima storms.

Figure 1 indicates that the only major sunspot group on the solar disk at the time of the two major flares was group number 12673 and the RGO reports state that the major flares originated from this group. Note, however, that the synthesized image (from the RGO drawings) in Figure 9b is 16.5 hrs before the flare erupts and that by 24 January (06:43 *UT*) the group 12673 is only just visible by its trailing edge on the eastern limb of the Sun.

The dominance the group 12673 at the time of the two flares is confirmed by Tables 1 and 2, for the first and second events, respectively. Table 1 shows that during the first event the total sunspot area (umbrae plus penumbrae, corrected for the foreshortening effect of the viewing geometry) of this group is 3370 *μsh* (where 1 *μsh* is a millionth of solar hemisphere), which is 85.6% of the total sunspot area on the Earth-side of the Sun at
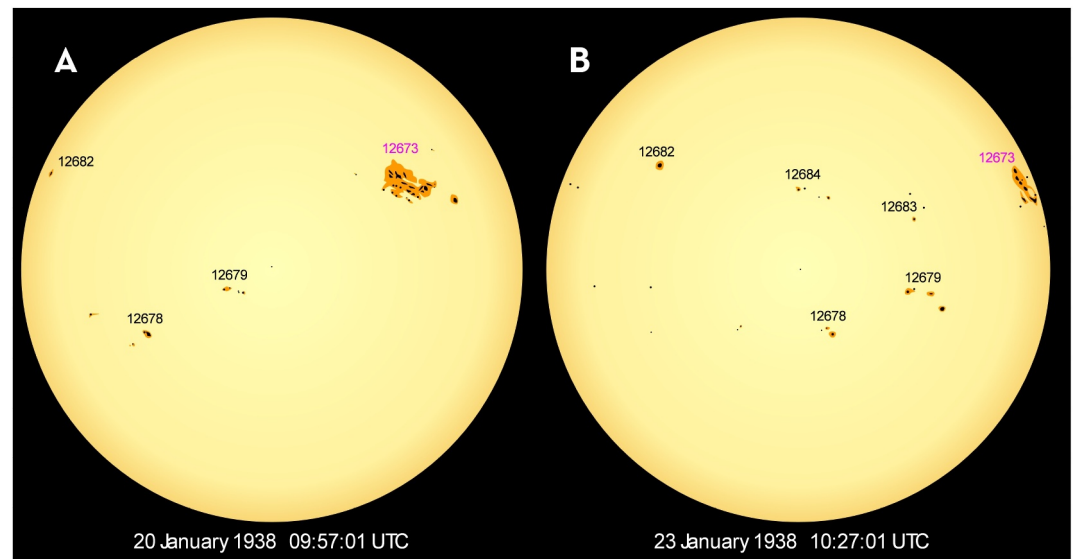
Figure 9. Synthesized solar white light images for the solar disk on (a) 20 January 1938 (at 09:57:01 *UT*) and (b) 23 January 1938 (at 10:27:01 *UT*), reconstructed from the Royal Greenwich Observatory (RGO) drawings. The major sunspot groups are numbered and group 12673 that generated the flares and Fátima storms is labeled in mauve. The images are, respectively, for 8hrs, 33min and 16hrs, 27min before the two major white light flares were seen by the RGO observers.

the time. The second largest group (AR13861) is just 197 μsh in total spot area, which is under 6% of the dominant group.

Table 2 shows that this dominance persists at the time of the second flare, although AR12673 has shrunk a little and is 2423 μsh in total spot area. This is still 80.2% of the total sunspot area on the visible disk, the only other sizable groups being AR12679 (180 μsh, which is 7.4% of the size of AR12673) and AR12682 (177 μsh, which is 7.3% of the size of AR12673). As can be seen in Figure 9b neither of these groups is close to the center of the solar disk at this time, but they are not on the limb like the dominant group.

5. The Origin of the Second Fátima Storm

The second Fátima storm is a highly significant event. Lockwood et al. (2025) show that it is 13th in the list of 21 extreme events in auroral extent. The solar observations at the time leave just two possibilities: (a) that it was

Table 1
Sunspot Groups on the Solar Disc on 20 January 1938

NOAA group number	Visible total area (μsh)	Corrected total area (μsh)	Area ratio to main group (%)	Latitude (north) (deg)	Carrington longitude (deg)	Distance from c.m. (deg)	Position angle (deg)
12672	3	17	0.50	26.40	236.40	37.40	312.90
12673	560	3,379	100.00	17.20	225.10	26.10	311.40
12675	0	7	0.20	18.20	211.90	12.90	331.70
12678	33	187	5.53	−19.80	158.70	−40.30	114.20
12679	16	75	1.47	−9.50	182.20	−16.80	105.90
12680	3	16	0.47	−11.80	151.90	−47.10	101.30
12681	8	53	1.57	−13.80	143.10	−55.90	103.30
12682	20	197	5.83	21.10	120.40	−78.60	67.70
	Total:	3,931					
	% main:	85.6					

Note. Areas are in millionths of a solar hemisphere and are corrected for fore-shortening; c.m. stands for central meridian.

Table 2
Sunspot Groups on the Solar Disc on 24 January 1938

NOAA group number	Visible total area (μsh)	Corrected total area (μsh)	Area ratio to main group (%)	Latitude (north) (deg)	Carrington longitude (deg)	Distance from c.m. (deg)	Position angle (deg)
12673	480	2,423	100.00	17.90	223.10	75.00	289.70
12678	17	80	3.3	−20.10	162.00	13.90	221.30
12679	29	180	7.40	−10.40	183.30	35.20	259.70
12682	35	177	7.30	20.50	118.90	−29.20	47.10
12683	5	18	0.74	6.80	182.30	34.20	289.30
12684	11	46	1.89	12.70	157.40	9.30	333.10
12685	6	24	0.99	−7.70	120.10	−28.00	96.30
12686	11	49	2.02	−13.30	98.60	−49.50	102.90
12687	3	6	0.24	−6.10	100.80	−47.30	93.30
12689	4	19	0.78	17.20	88.80	−59.30	67.50
	Total:	3,022					
	% main:	80.2					

Note. Areas are in millionths of a solar hemisphere and are corrected for foreshortening; c.m. stands for central meridian.

caused by a CME launched from the dominant active region on the limb or (b) it was caused by a CME launched from closer to the limb centre and any associated flare was not detected (the lack of detection would not be surprising as X-ray and EUV observations were not available at the time). There are two possibilities to consider for option (b): that it was caused by a CME launched from one of the small active regions or that it did not originate from an active region at all. Zhang et al. ([2007](#)) surveyed 88 major geomagnetic storms (defined by minima in the *Dst* index of −100 *nT* or less) that occurred during 1996–2005. For the 85 events for which the surface source regions could be investigated, 54 (63%) of the storms originated in solar active regions, 11 (13%) in quiet Sun regions associated with quiescent filaments or filament channels, and 11 (13%) were associated with coronal holes. In addition, there were 9 (11%) CME-driven events showed no sign of eruptive features on the surface or in the low corona (e.g., no flare, no coronal dimming, and no loop arcade, etc.), even though all the available solar observations in a suitable time period were carefully examined: these are known as "stealth CMEs." Figure 8 of Zhang et al. ([2007](#)) shows the source locations on the solar disk of the events they surveyed and 56 of the 65 source identified regions (86%) lie within 45° from central meridian, 49 (75%) within 30°, and 34 (52%) within 15°. Hence the vast majority of major storms arise from solar sources that are close to central meridian. The sources also show an east-west asymmetry that strongly favors the western hemisphere. We note one event in their survey, on 18 April 2001, arose from an active region (AR6415) just before it rotated off the solar disk on the western limb (when) it had an area of 599 *μsh*. This generates a moderately large geomagnetic storm in which *Dcx* fell to −83*nT*.

Table 3 lists all the storms generated by stealth CMEs that we found in the literature. There are 16 of them and they are in the interval 2010–2018. In comparison, the database compiled by Cane and Richardson ([2003](#)) and Richardson and Cane ([2010](#)) (updated version published with https://doi.org/10.7910/DVN/C2MHTH) contains 187 CMEs at Earth in this interval and so Table 3 contains about 8.5% of CMEs at Earth in this interval.

The table lists the events by their arrival time at Earth and gives the minimum of the *Dcx* index during the subsequent geomagnetic disturbance. It can be seen that the geomagnetic storms caused are generally small, the largest being −175*nT*. For the larger events it is likely that the stealth CME was slow and was enhanced by a second CME that followed it, as discussed by Yardley et al. ([2021](#)). All of these events are considerably smaller in magnitude than the −336 *nT* of the second Fátima storm: hence if that storm was caused by a stealth CME, it had twice the geoeffectiveness of any of the stealth CMEs seen in recent years.

Another possibility is that the CME in the second Fátima storm arose from one of the smaller active regions on the disk at the time. These ARs were all smaller than 180 *μsh* in total spot area. We surveyed the storms that arose from CMEs from ARs smaller than 200 *μsh* for the same interval as the stealth CME list (2010–2018). This was done using the searchable DONKI database (Space Weather Database Of Notifications, Knowledge, Information,

Table 3
Geomagnetic Disturbances Caused by Stealth Coronal Mass Ejections

Date of Peak storm	Minimum Dcx (nT)	Reference
21 June 2010	−5	Nitta and Mulligan (2017)
28 December 2010	−50	Nitta and Mulligan (2017)
24 January 2011	−10	Nitta and Mulligan (2017)
4 February 2011	−71	Nitta and Mulligan (2017)
7 March 2011	−30	Nitta and Mulligan (2017)
30 March 2011	−2	Nitta and Mulligan (2017)
28 May 2011	−95	Nitta and Mulligan (2017)
9 October 2012	−111	Nitta and Mulligan (2017)
1 June 2013	−105	Nitta and Mulligan (2017)
7 June 2013	−70	Nitta and Mulligan (2017)
29 June 2013	−88	Nitta and Mulligan (2017)
6 July 2013	−80	Nitta and Mulligan (2017)
7 January 2015	−112	Yardley et al. (2021), Nitta et al. (2021)
10 October 2016	−121	He et al. (2018), Nitta et al. (2021)
28 May 2017	−122	Nitta et al. (2021)
26 August 2018	−175	Mishra and Srivastava (2019), Nitta et al. (2021)

https://kauai.ccmc.gsfc.nasa.gov/DONKI/), developed at the Community Coordinated Modeling Center. This yielded the 10 storms listed in Table 4, which is just 5.3% of the number of CMEs at Earth in the Cane and Richardson catalog.

Table 4 shows that the geomagnetic storms caused by CMEs launched from ARs smaller than 200 μsh in total spot area are rare and generally very weak. The largest is less than a half of the magnitude of the second Fátima storm.

We conclude from this analysis that the second Fátima storm could have been caused by a CME from one of the smaller active regions on the disk or by a stealth CME that has no obvious source. However, this would make the second Fátima storm very unusual because in recent years no such storm has exceeded half the magnitude of the second Fátima storm.

Table 4
Geomagnetic Disturbances Caused by Coronal Mass Ejections From Small Active Regions of Total Area ≤180 μsh

CME date	Source AR NOAA #	AR area (μsh)	Propagation time to 1AU (hr)	Date of peak storm	Minimum Dcx (nT)
3 April 2010	11059	43	41.1	6 April 2010	−81
7 August 2010	11093	191	58.6	10 August 2010	−25
7 June 2011	11226	55	57.3	9 June 2011	−33
10 March 2012	11430	141	46.0	12 March 2012	−53
27 September 2012	11577	19	45.0	30 September 2012	−120
7 January 2014	11943	25	30.6	9 January 2014	−18
29 March 2014	12017	200	79.6	2 April 2014	−2
1 July 2014	12106	119	48.3	3 July 2014	−16
13 May 2015	12345	12	99.3	18 May 2014	−40
16 December 2015	12468	23	57.5	21 December 2014	−152
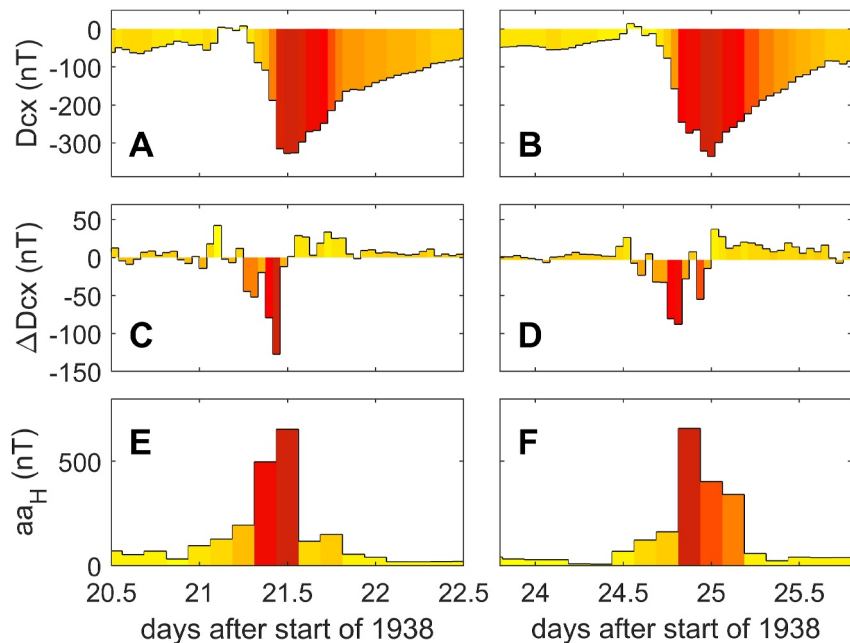
Figure 10. Detail of the geomagnetic disturbances in the Fátima storms. Parts (a) and (b) show the *Dcx* index variation in the first and second storms of January 1938, respectively. Parts (c) and (d) show the change in *Dcx* from 1 hr to the next, Δ*Dcx*. Parts (e) and (f) show *aa$_H$*. All panels cover intervals 2 days long.

6. Substorms During the Fátima Storms

The continuous AE indices (AE), used to identify substorms phenomena, are not available until 1964 (Davis & Sugiura, 1966). The *aa$_H$* index responds to substorms (Lockwood et al., 2019), but has a 3 hr resolution which means individual substorms are not detected. In this paper, we look at the rate of change of the *Dcx* index, Δ*Dcx*, the change between one hourly value and the next:

$$\Delta Dcx = Dcx(t + 1) - Dcx(t) \qquad (4)$$

Studies using the *Dst* index, that is similar to *Dcx*, show that substorms are associated with large negative spikes in Δ*Dst*, as particles are injected into the ring current by substorms (Ohtani et al., 2001; Partamies et al., 2013).

Figure 10 shows the variations of Δ*Dcx* and *aa$_H$* and do identify several negative spikes in Δ*Dcx* that are at times of elevated *aa$_H$*, and so are very likely to reveal substorm occurrence. This is further investigated in the next section that looks at the Halloween storms of 2003 for which we have not only the northern-hemisphere AE indices but also the SuperMAG SME indices that are compiled using the same methodology as AE, but from a considerably larger number of northern hemisphere stations (Newell & Gjerloev, 2011a, 2011b).

7. The Halloween Storms

Figure 11 shows the Halloween storms in the same format as Figure 1. It can be seen that there are some similarities to the Fátima events but also considerable differences. There is a dominant sunspot group on the solar disk (NOAA number 10486) but this time there are other groups of considerable area present as well. Nevertheless the flare activity is all from that dominant group.

Flares were detected in EUV and X-rays, instead of the white light in which the Fátima event flares were seen. We use flare peak times (rather than onset times) as that was what was recorded for the Fátima event. The first flare was an X5.4 that peaked at 08:35 *UTC* on 23 October (day-of-year, d-o-y) 295 for the definition used that d-o-y is zero at 00UT on 1 January): this first event was the weakest flare of the sequence and is not shown in Figure 11. The second was an X17.2 flare that peaked at 11:10 *UTC* on 28 October (d-o-y 300 and seen in part (c) of Figure 12): this was the second largest flare in the sequence and was associated with a fast CME (speed of order
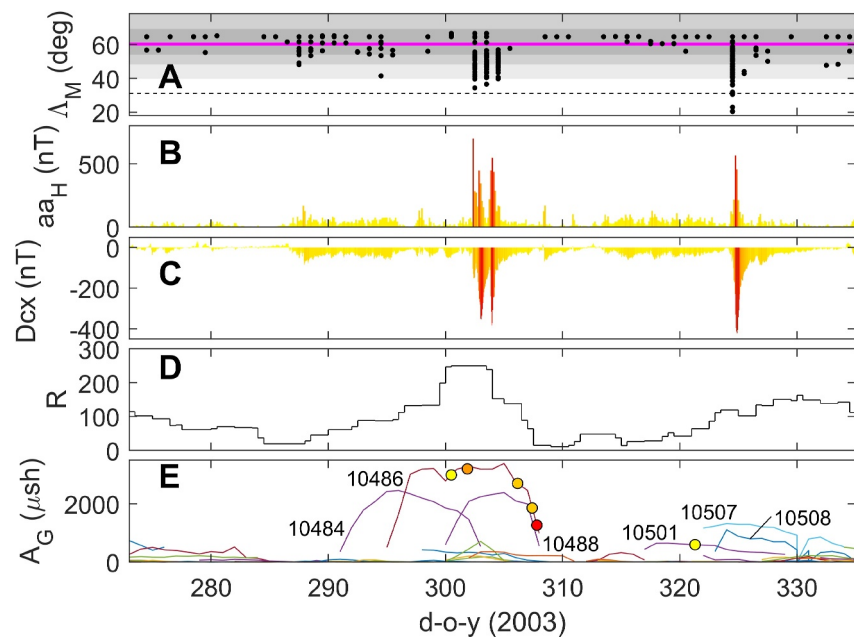
Figure 11. Same as Figure 1 for the Halloween storms of October/November 2003.

2125 km s^{-1}) that reached Earth at 6 UT on 29 October (d-o-y 301), giving a small positive ΔDcx enhancement, approximately 19 hr after the peak of the flare (a considerably lower propagation time than for the Fátima events). This caused a string of 3 substorms in rapid succession seen on d-o-y 301 in parts (c), (e) and (g) of Figure 13. We use the SuperMAG *SML* index Newell and Gjerloev (2011b); Newell and Gjerloev (2011a) to identify substorms which is the largest negative disturbance seen by any northern hemisphere magnetometer station and is the equivalent of the AL index or the AE Davis and Sugiura (1966). The substorms caused by this CME give minima in *SML* of $-3{,}180$, $-3{,}596$, and $-3{,}645$ *nT* in a 25-min period. However, this did not generate a geomagnetic storm, as there was only a weak minimum in *Dcx* (part d). There was subsequently weaker X10.0 and X8.3 flares. The associated CMEs had an accumulative effect on *Dcx* by generating multiple weaker substorms and then a strong substorm and second minimum in *Dcx*. These effects of multiple CME impacts are not seen in the Fátima events, which appear to have been caused by a single CME in both cases. Just after sunspot group 10486 had rotated off the eastern limb it generated a massive flare, estimated to be between X28 and X45. This is the largest flare ever recorded and the GOES (Geostationary Operational Environmental Satellite) detectors saturated, which is why the precise magnitude is not known (Tokumaru et al., 2005; Watari, 2022). This flare is very close to the eastern solar limb, like that in the second Fátima event, but unlike in the 1938 events, this CME did not impact Earth and hence it did not generate a geomagnetic storm, as can be see in part (c) of Figure 11.

There was one other event in the Halloween storm series that followed during the next Carrington rotation and can be seen in Figure 11. This originated from sunspot group with NOAA number 10501. This generated a M1.4-class flare with a narrow, slow CME and a M9.6-class flare with a fast, full-halo CME. The latter CME was particularly geoeffective and generated a geomagnetic storm on 20 November (d-o-y 323 in Figure 11) in which *Dcx* fell to -418 *nT* (and *Dst* to -472 *nT*) and generated an auroral event that Lockwood et al. (2025) estimate to be the seventh most extensive recorded. This event is shown in detail in the right-hand panels of Figure 13.

Figure 12 shows some images associated with the two major flares that emerged from NOAA sunspot group number 10486 during the Halloween storms. These flares can be seen in parts (c) and (d) in the southern solar hemisphere, just west of the central meridian and at the eastern limb, respectively. Parts (a) and (b) confirm that these flares originated from group 10486. The bottom panels (e) and (f), respectively, show the LASCO coronagraph images of the associated CME. It can be seen in (e) the CME is a halo form that will hit Earth but that in (f) the CME is propagating towards the right in the image and does not extend over the Sun-Earth line. As a result, this CME missed Earth and did not generate a geomagnetic storm.
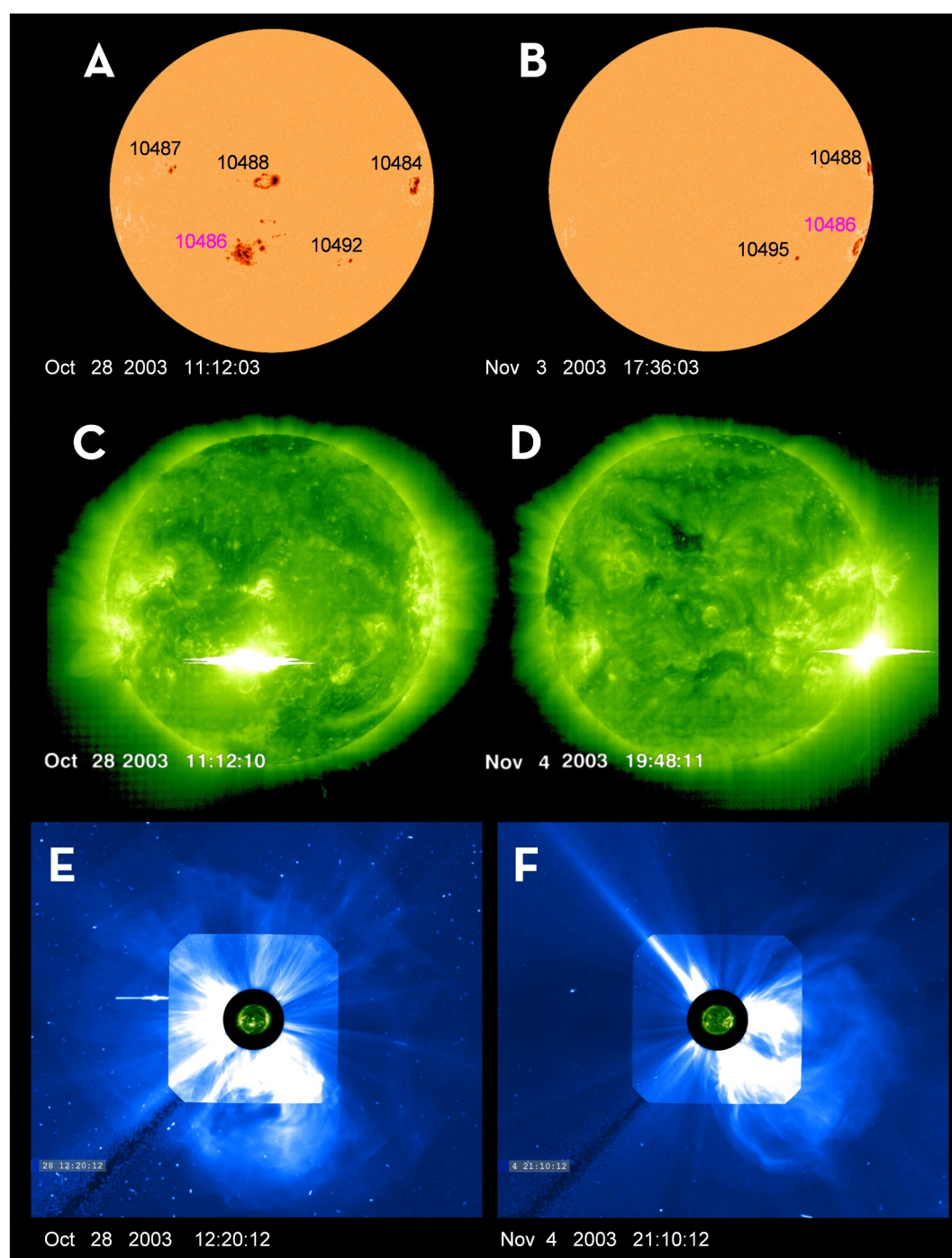
Figure 12. Solar/heliospheric images relating to the Halloween Storms of October/November 2003. (a), (c), and (e) relate to the Coronal Mass Ejection (CME) associated with the flare seen in the SoHO/EIT image for 28 October 2003 (d-o-y 300) at 11:12:10 UTC shown in (c), whereas (b), (d), and (f) relate to the huge flare seen on the limb in part (d), the corresponding EIT image for 4 November 2003 (d-o-y 307) at 19:48:11 UTC. Part (a) and (b) are white light continuum images from the SoHO/MDI instrument for, respectively, 7 s and 26 hr, 12 min before the flares. In relation to (b), the causal sunspot group 10486 (numbered in mauve) is present in the MDI magnetograph data until 23:59:53 UTC (4 hr, 12 min after the second flare) but is harder to see on the limb in the continuum images. Part (e) and (f) are composite SoHO/LASCO coronagraph images of the CMEs associated with the flares.
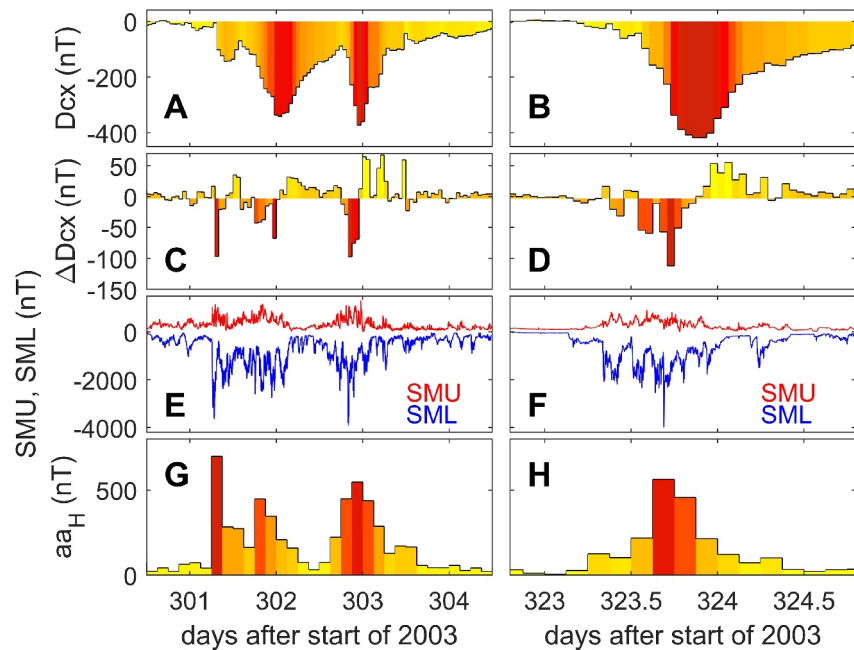
Figure 13. Detail of the geomagnetic disturbances in the Halloween storms. The second (parts c and d) and fourth panels (parts g and h) correspond to the second and third panels in Figure 10 between them parts (e) and (f) are inserted showing the SuperMAG SME indices, *SMU* (in red) and *SML* (in blue) and the top panels (parts a and b) show the *Dcx* index. The left-hand parts (a), (c) (e), and (g) cover the 4-day interval of the Halloween storms whereas the right-hand parts. (b), (d), (f), and (h) cover a 2 day interval (as in Figure 10), which contains the subsequent 20 November storm.

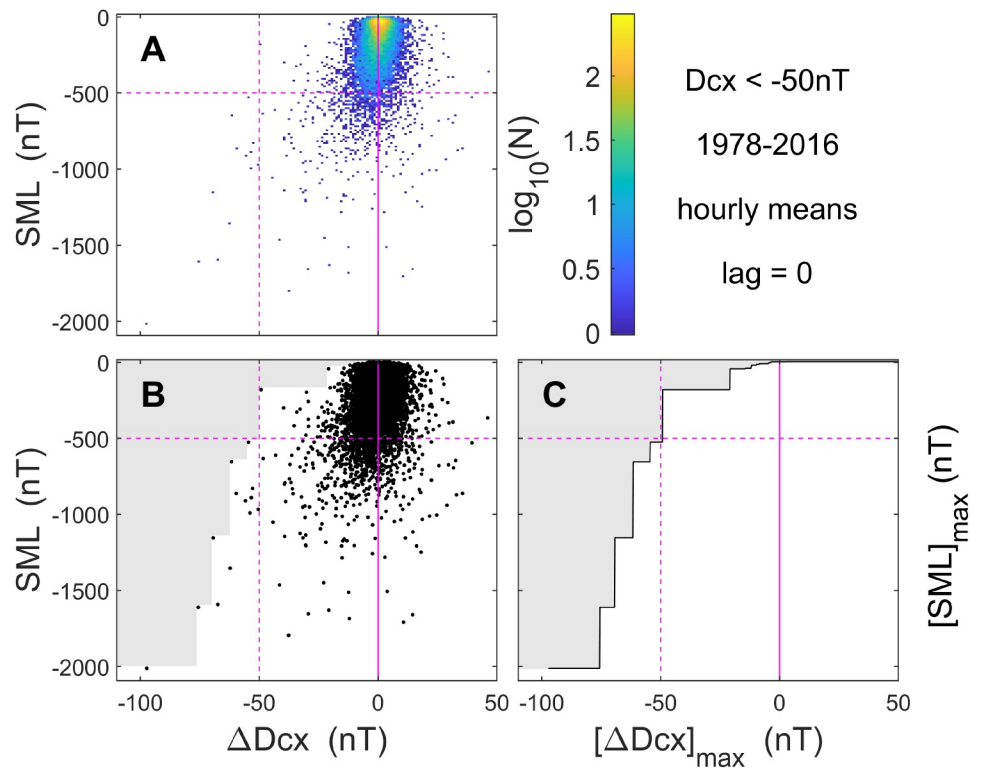## 8. The Relationship Between Substorms, Ring Current Enhancements and Low-Latitude Aurora

Figures 10 and 13 show that both the Fátima and Halloween storms are characterized by large enhancement events in the ring current (large negative spikes in ΔDcx). The purpose of this section is to test the relationship of these events to substorms. We have no direct measure of substorm activity for the Fátima events but the *SML* index shown in parts (e) and (f) of Figure 13 does show that in the Halloween storms these large negative ΔDcx events are associated with substorms, as identified in the *SML* index. We here take a more general look at this relationship, using the simultaneous *Dcx* and *SML* hourly averages that are available for 1978–2016, inclusive.

We have continuous and simultaneous *Dcx* and *SML* data for the years 1978–2016 (inclusive), a total of 341,880 hourly averages. Of these data, there are 17,861 samples (5.2% of total) with $Dcx \leq -50nT$ and we here define "storm-time" samples of ΔDcx as having *Dcx* below $-50nT$. A lag correlogram of these 17,861 storm-time hourly *SML* and ΔDcx samples shows that peak correlation is at zero lag and the correlation coefficient is $r = 0.311$ (with a maximum of 0.325 and a minimum of 0.298 at the 2-sigma uncertainty level). The *p* value of the null hypothesis is too small to quantify, because of the very large number of samples. Hence the correlation is weak but significant. Because it is weak, rather than use the correlation, we here investigate the largest *SML* (lowest substorm activity level, $[SML]_{max}$) for a given ΔDcx.

Figure 14a is a "data density plot" (i.e., a two-dimensional histogram) in which the numbers *N* of storm-time samples ($Dcx \leq -50nT$) in bins are color coded, according to a logarithmic scale, as a function of *SML* (along the vertical axis) and the change in *Dcx*, ΔDcx (along the horizontal axis). A total of 11,959 of the 17,861 storm-time data pairs give $SML < -500nT$ (the horizontal dashed mauve line) and of these 70.2% correspond to negative ΔDcx. As we move to less negative *SML* (lower activity levels) part A shows this fraction decreases, such that only 37.8% of the 8,304 samples for $SML \leq -10nT$ give negative ΔDcx. Hence, for storms with $Dcx \leq -50nT$, whereas large negative *SML* tends to give negative ΔDcx, for weak auroral activity ($SML > -10nT$) there tends to be positive ΔDcx which means the ring current is the recovering from events of large negative ΔDcx that occurred before it.
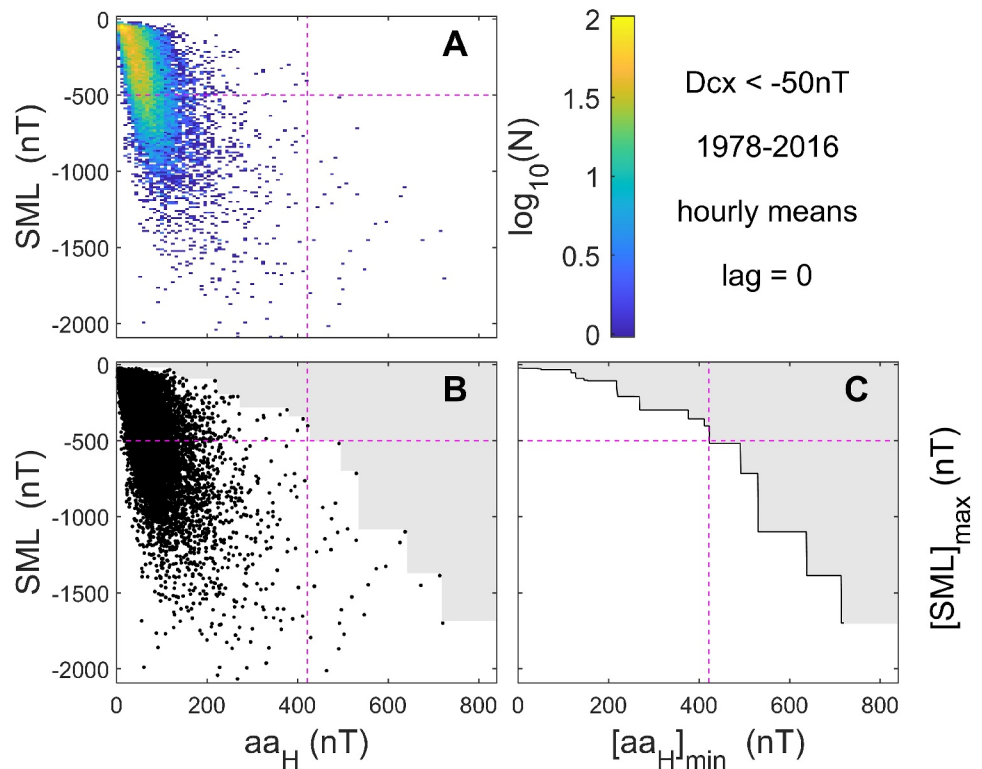
Figure 14. Analysis of the relationship between storm-time changes in the *Dcx* index and the auroral substorm *SML* index for 1978–2016, inclusive. From 341,880 hourly averages, 17,861 (5.2%) have $Dcx \leq -50 nT$ and are classed as "storm-time." Part (a) is a "data density plot" (a two-dimensional histogram) in which the numbers of these storm-time samples (N) in bins are color coded (on a log scale) as a function of *SML* (along the vertical axis) and the subsequent change in *Dcx*, ΔDcx (along the horizontal axis) for bins that are 1 nT wide in *SML* and 12 nT wide in ΔDcx. Part (b) is a scatter plot of the same data. There are no data in the gray area. Part (c) plots the delineator of the gray area in (b), showing the maximum value of *SML* (i.e., the lowest disturbance level) for a data subset defined by $\Delta Dcx \leq [\Delta Dcx]_{max}$ (i.e., a disturbance change level equal to or greater than $[\Delta Dcx]_{max}$) for these data with $Dcx \leq -50 nT$.

During the large storms of the Fátima and Halloween events, ΔDcx falls below the $-50 nT$ level in the large negative spikes seen in Figures 10 and 13, and it is the relation of these large negative ΔDcx events to substorms that we wish to investigate.

In the first Fátima event (Figure 10c) the large negative ΔDcx values (colored in orange, red or deep red) were -52.03, -79.46, and -127.56 nT: these 3 values are all to the left of the vertical dashed mauve line in all three parts of Figure 14. All three panels stress that there are no hourly averages of *SML* above (i.e., less disturbed) than -500 nT for these magnitudes of ΔDcx. Indeed for these three values of ΔDcx the maximum *SML* is -633, -1992, and -1992 nT. These are the maximimum hourly values. To put these numbers into context, consider the isolated large negative ΔDcx spike during the event at the end of the Halloween storm sequence seen on d-o-y 323 in Figure 13d. This gives ΔDcx of -97.2 nT for which $[SML]_{max}$ is -1992 nT (hourly value). Looking at the 1-min resolution *SML* data we find that this hourly value was set by a single substorm in which *SML* fell to $-3,960$ nT. Hence, we can infer that the large negative ΔDcx spikes shown in red in Figure 10c were accompanied by significant substorm activity.

Similarly in the second Fátima event. Figure 10d shows negative spikes in ΔDcx of -80.75, -87.88, and -55.14 nT. These give $[SML]_{max}$ of -1992, 1992, and -1135 nT, again, identifying significant substorm activity.

We have performed the same analysis using the aa_H index values, as shown in Figure 15. Hourly aa_H values were generated from the 3-hourly data by linearly interpolating to the times of the hourly *SML* data. These aa_H values and the hourly means of *SML* are anti-correlated, with peak correlation at zero lag of $r = -0.620$ with a 2-σ uncertainty range between -0.630 and -0.611. The probability of the null hypothesis is again effectively zero. The intervals in the Fátima storms that are colored red or deep red in Parts (c) and (d) of Figure 10 have aa_H

Figure 15. Analysis of the relationship between storm-time ($Dcx \leq -50nT$) values of the aa_H index and the auroral substorm *SML* index for 1978–2016, inclusive, in the same format as Figure 14. Hourly values of aa_H are generated by linearly interpolating the 3-hourly values to the times of the hourly SML data. The data density plot in Part (a) is for bins that are 1 nT wide in *SML* (vertical axis) and 8 nT wide in aa_H (horizontal axis). The scatter plot in Part (b) again shows where there are no data in the gray area and Part (c) shows the maximum value of *SML* (i.e., the lowest disturbance level) for a data subset defined by $aa_H \geq [aa_H]_{min}$ (i.e., a greater disturbance level than $[aa_H]_{min}$).

exceeding 422 nT (the vertical mauve dashed lines in Figure 10) which again reveals that *SML* is more negative than $-500\,nT$ and likely to be a lot lower.

The linear correlation between aa_H and *SML* is not especially high, but a linear regression fit yields fitted *SML* values for the peak values in 3-hourly aa_H of $-1{,}200 \pm 221$ and $-1{,}476 \pm 230\,nT$ for the first Fátima event and $-1{,}485 \pm 230$ and $-1{,}125 \pm 220\,nT$ for the second. Applying the same regression to the aa_H peaks in the Halloween events yields $-1{,}622 \pm 238$, $-1{,}157 \pm 220$, $-1{,}259 \pm 222$, and $-1{,}285 \pm 222\,nT$. From the data shown in Panels (e) and (f) of Figure 13 the actual minima in hourly *SML* during these peaks of activity are $-1{,}742$, $-1{,}685$, $1{,}966$, and $-1{,}864\,nT$. Hence the linear regression using aa_H tends to underestimate the observed hourly means of *SML* and, of course, considerable underestimate the minimum values in the 1-min data. Nevertheless, this simple analysis of the aa_H data supports the conclusion from the *Dcx* that during the Fátima storms there was very strong substorm activity. This is no surprise as previous studies have found that the red aurora that appears during storms at lower latitudes occurs when a sequence of magnetospheric substorms is in progress, as demonstrated by Tinsley et al. (1986), Miyaoka et al. (1990), Rassoul et al. (1992), and Shiokawa et al. (1994).

9. Discussion and Conclusions

This paper has investigated the Fátima storms of 1938 using comparisons to modern data to try to elucidate the substorm and CME behavior.

The Halloween storms of 2003 provide an interesting comparison. During the first Fátima storm and the first major Halloween storm, the geomagnetic disturbance levels in *Dcx* and aa_H were similar but the first Fátima storm appears to have been driven by a single CME impact that caused a series of substorms of increasing

magnitude, whereas the Halloween storms showed the accumulated effect of a series of CME impacts. In both cases, the sunspot group responsible later produced a major flare just after its main part had passed around the western limb of the Sun. In the case of the 2003 events, the CME associated with this flare missed the Earth, as is commonly assumed would be the case. However, in the case of the second Fátima storm, if the flare was the source the CME must have been broad enough in width to impact the Earth. This was not just a glancing blow because it generated the second Fátima storm, which was similar in magnitude to the first one.

Given the data we have, it is not possible to be definitive about the source of the second Fátima storm in January 1938. However, we can narrow it down to two options; both of which make the event very unusual. The first is that the event arose from a small active region (total surface sunspot area below $180\,\mu sh$) or from a stealth CME (that has no obvious source feature in either the photosphere or the corona) from closer to the centre of the visible disk. Analysis of 8 year's data presented in this paper suggests that the largest storm that these can generate is about half the magnitude of the second Fátima storm, as quantified using the geomagnetic Dcx index. However, this is based on a comparison with modern data from just 8 years. The scale of the anomaly in invoking an unseen CME source near the disk center is perhaps best demonstrated by the latitude extent of the auroral observations. The second Fátima storm reached down to an observer at a QD geomagnetic latitude Λ_M of $26.48°$ which means it ranks as 13 in a list of 21 events that meet the $\Lambda_M = 31°$ threshold for extreme events adopted by Lockwood et al. (2025). In all of these events the associated active region was greater in total surface area than $500\,\mu sh$. Events 12 and 14 in that ranked list are the events on 11 February 1958 and 25 September 1909 which are linked with, respectively, active regions 18,502 (area $999\,\mu sh$) and 6,727 (area $691\,\mu sh$) that were both quite close to the center of the solar disk. However the regions on 24 January 1938 near to the disc center were 12679 (area $180\,\mu sh$) and 12682 (area $177\,\mu sh$) and so considerably smaller.

The alternative explanation is that the large group 12673 (area $2423\,\mu sh$) is responsible even though it was very close to the solar limb. We know that this group was the source of a very large flare at a time that is fully consistent with the timing of the geomagnetic storm. CME eruptions from the limb quite often generate geomagnetic disturbances but these are usually weak because the shock front intersects the Earth but the CME itself does not, events that are often called "driverless interplanetary shocks" (Gopalswamy, Mäkelä, et al., 2009; Gopalswamy, Yashiro, et al., 2009; Gopalswamy et al., 2010). However, the event on 18 April 2001 in the survey by Zhang et al. (2007) that arises from AR9415 is an example of an event originating from the western solar limb from which both a shock and the driver CME are seen at Earth, yielding a moderate geomagnetic storm. For this to happen, we require the CME to be very wide in its heliographic longitude extent and/or it to be deflected towards the Earth in azimuthal (longitudinal) direction. The greatest longitudinal extent $(\Delta\phi_H)$ of a CME known is an event on 1 August 2010, for which $\Delta\phi_H \geq 120°$, which was seen passing over the Wind craft at L1, MESSENGER (at $0.38\,AU$), Venus Express (at $0.72\,AU$) to Wind, ACE, and ARTEMIS near Earth and both the STEREO-A and STEREO-B craft and the width was confirmed using the Heliospheric Imagers on those craft (Möstl et al., 2012). This event drove a moderately large geomagnetic storm with Dcx falling to a minimum of $-85\,nT$. Other studies have found very wide CMEs using combinations of in situ data, heliospheric imagers and modeling (Lugaz et al., 2008; Möstl et al., 2010). For a radially-propagating and symmetric CME launched from the limb to reach Earth its width $\Delta\phi_H$ would need to exceed $180°$, something we have not seen in modern times with spacecraft or imagers, However this width requirement would be reduced if the CME were deflected from the radial towards Earth. The fact that geoeffective CMEs hitting Earth predominantly originate from the western half of the solar disk (Wang et al., 2004; Zhang et al., 2007) strongly suggests a persistent azimuthal deflection towards Earth for CMEs launched from the western limb which is consistent with a pressure build-up for a CME moving faster than the background solar wind and the Parker spiral configuration. Furthermore, analysis and modeling shows CMEs are deflected away from open flux regions (Gopalswamy, Mäkelä, et al., 2009; Kay et al., 2017). For sunspot minimum conditions, with open flux in the polar coronal holes, this deflection will be largely latitudinal towards the solar equator. However, the Fátima storms are roughly a year after sunspot maximum and so there is longitudinal as well as latitudinal structure in the open-closed boundaries and so open flux will also cause longitudinal deflections. In particular, a CME erupting just to the east of a trailing edge of a lower-latitude coronal hole will be subject to stronger westward deflection.

If the second Fátima storm is caused by an exceptionally wide (in longitude) and deflected CME that arose with the observed limb flare it is certainly a rare event. Because we know of nothing else like it, it appears to be at least a once-in-a-hundred-years event. If, on the other hand, it was caused by a CME from nearer the center of the disc

(that, by coincidence, is very close in time to the large limb flare) it is of considerably greater magnitude than anything we have seen in modern time for flares from small active regions ($\leq$180 μsh) or for stealth CMEs.

That the first possibility remains means it needs to be considered when making forecasts for operations. For example, when executing a controlled de-orbiting of a large defunct spacecraft such as ENVISAT or, when decommissioned, the ISS or of any large piece of space junk, one needs to be certain that a major storm will not occur and heat the thermosphere (Lockwood, 2025). The second Fátima storm may be an example where a major storm was generated by an active region that had largely passed beyond the eastern limb of the Sun. Because an unexpected event of the scale of the Fátima storms would render such a re-entry effectively uncontrolled with serious consequences, it is important to consider this as a possibility even though it would be a very rare event.

We have also shown that the Dcx index, allied to the aa_H index, gives us a way of identifying large substorms in events back to 1932. In the case of the Fátima storms, Figure 10 implies that the first Fátima event comprised a series of four substorms in close succession and of increasing magnitude. On the other hand, the second Fátima event involved two, possibly 3, large substorm cycles in quick succession followed by two more smaller ones after a delay of about 6 hr which added to the duration of the event but not its peak magnitude.

Analysis of the auroral records shows that the geographic longitudes where low-latitude aurora was observed during the Fátima events were different in the two events because the Universal Time of the arrival of the two CMEs at Earth was different.

Data Availability Statement

The auroral records used here were all obtained from previous publications, in particular from the paper by Hayakawa et al. (2021) and Lockwood et al. (2025). The sunspot data used were generated by WDC-SILSO/SIDAC, Royal Observatory of Belgium, Brussels and are available from https://www.sidc.be/SILSO/datafiles. The sunspot group areas and drawings were retrieved from the Debrecen Photoheliographic Database http://fenyi.solarobs.epss.hun-ren.hu/en/databases/DPD/. The definitive Dcx index (at the time of writing, up to the end of 2016) is available from Oulu University at http://dcx.oulu.fi/?link=queryDefinite and provisional Dcx from http://dcx.oulu.fi/?link=queryProvisional. The homogeneous aa_H geomagnetic index is stored in the supplementary information files attached to the papers by Lockwood, Chambodut, et al. (2018) and Lockwood, Finch, et al. (2018). The images of Sun during the Halloween events are available from the SoHO data archive at https://soho.nascom.nasa.gov/data/archive/.

References

Alken, P., Thébault, E., Beggan, C. D., Amit, H., Aubert, J., Baerenzung, J., et al. (2021). International geomagnetic reference field: The thirteenth generation. *Earth Planets and Space*, 73(1), 49. https://doi.org/10.1186/s40623-020-01288-x

Anonymous. (1938). Aurora of january 25-26 (news and views). *Nature*, 141(3561), 192. https://doi.org/10.1038/141192b0

Brodrick, D., Tingay, S., & Wieringa, M. (2005). X-ray magnitude of the 4 November 2003 solar flare inferred from the ionospheric attenuation of the galactic radio background. *Journal of Geophysical Research*, 110(A9), 2004JA010960. https://doi.org/10.1029/2004JA010960

Cane, H. V., & Richardson, I. G. (2003). Interplanetary coronal mass ejections in the near-Earth solar wind during 1996–2002. *Journal of Geophysical Research*, 108(A4). https://doi.org/10.1029/2002ja009817

Carcaboso, F., Dumbović, M., Kay, C., Lario, D., Jian, L. K., Wilson Iii, L. B., et al. (2024). Unveiling the journey of a highly inclined CME: Insights from the March 13, 2012, event with 110° longitudinal separation. *Astronomy & Astrophysics*, 684, A90. https://doi.org/10.1051/0004-6361/202347083

Cid, C., Cremades, H., Aran, A., Mandrini, C., Sanahuja, B., Schmieder, B., et al. (2012). Can a halo cme from the limb be geoeffective? *Journal of Geophysical Research*, 117(A11). https://doi.org/10.1029/2012JA017536

Cliver, E. W., & Crooker, N. U. (1993). A seasonal dependence for the geoeffectiveness of eruptive solar events. *Solar Physics*, 145(2), 347–357. https://doi.org/10.1007/BF00690661

Cowley, S. W. H., & Lockwood, M. (1992). Excitation and decay of solar wind-driven flows in the magnetosphere-ionosphere system. *Annales Geophysicae*, 10, 103–115. Retrieved from https://ui.adsabs.harvard.edu/abs/1992AnGeo..10..103C(ADSBibcode:1992AnGeo..10..103C)

Daglis, I., Thorne, R., Baumjohann, W., & Orsini, S. (1999). The terrestrial ring current: Origin, formation, and decay. *Reviews of Geophysics*, 37(4), 407–438. https://doi.org/10.1029/1999rg900009

Davis, T., & Sugiura, M. (1966). Auroral electrojet activity index *AE* and its universal time variations. *Journal of Geophysical Research*, 71(3), 785–801. https://doi.org/10.1029/JZ071i003p00785

Ebihara, Y., & Ejiri, M. (2003). Numerical simulation of the ring current: Review. *Space Science Reviews*, 105(1/2), 377–452. https://doi.org/10.1023/a:1023905607888

Frederico, G. (2023). *How many people on earth? World population 1800–1938 (technical report no. Working papers in economic history)*. Universidad Carlos III de Madrid. Instituto Figuerola. Retrieved from https://ideas.repec.org/p/cte/whrepe/36431.html

Gopalswamy, N., Mäkelä, P., Xie, H., Akiyama, S., & Yashiro, S. (2009). CME interactions with coronal holes and their interplanetary consequences. *Journal of Geophysical Research*, 114(A3), 274. https://doi.org/10.1029/2008ja013686

Gopalswamy, N., Mäkelä, P., Xie, H., Akiyama, S., Yashiro, S., Maksimovic, M., et al. (2010). Solar sources of "driverless" interplanetary shocks. In *AIP conference proceedings* (pp. 452–458). AIP. https://doi.org/10.1063/1.3395902

Gopalswamy, N., Yashiro, S., Liu, Y., Michalek, G., Vourlidas, A., Kaiser, M. L., & Howard, R. A. (2005). Coronal mass ejections and other extreme characteristics of the 2003 October–november solar eruptions. *Journal of Geophysical Research*, *110*(A9). https://doi.org/10.1029/2004JA010958

Gopalswamy, N., Yashiro, S., Michalek, G., Stenborg, G., Vourlidas, A., Freeland, S., & Howard, R. (2009). The SOHO/LASCO CME catalog. *Earth, Moon, and Planets*, *104*(1–4), 295–313. https://doi.org/10.1007/s11038-008-9282-7

Gosling, J. T., Thomsen, M. F., Bame, S. J., & Zwickl, R. D. (1987). The eastward deflection of fast coronal mass ejecta in interplanetary space. *Journal of Geophysical Research*, *92*(A11), 12399–12406. https://doi.org/10.1029/ja092ia11p12399

Grandin, M., Bruus, E., Ledvina, V. E., Partamies, N., Barthelemy, M., Martinis, C., et al. (2024). The geomagnetic superstorm of 10 may 2024: Citizen science observations. *EGUsphere*, *2024*, 1–32. https://doi.org/10.5194/egusphere-2024-2174

Hady, A. (2009). Descriptive study of solar activity sudden increase and Halloween storms of 2003. *Journal of Atmospheric and Solar-Terrestrial Physics*, *71*(17–18), 1711–1716. https://doi.org/10.1016/j.jastp.2008.11.019

Hayakawa, H., Ebihara, Y., Mishev, A., Koldobskiy, S., Kusano, K., Bechet, S., et al. (2025). The solar and geomagnetic storms in 2024 may: A flash data report. *Ap J*, *979*(1), 49. https://doi.org/10.3847/1538-4357/ad9335

Hayakawa, H., Hattori, K., Pevtsov, A. A., Ebihara, Y., Shea, M., McCracken, K., et al. (2021). The intensity and evolution of the extreme solar and geomagnetic storms in 1938 January. *The Astrophysical Journal*, *909*(2), 197. https://doi.org/10.3847/1538-4357/abc427

He, W., Liu, Y. D., Hu, H., Wang, R., & Zhao, X. (2018). A stealth CME bracketed between slow and fast wind producing unexpected geo-effectiveness. *The Astrophysical Journal*, *860*(1), 78. https://doi.org/10.3847/1538-4357/aac381

Jones, H. (1955). *Sunspot and geomagnetic-storm data derived from greenwich observations 1874-1954 (technical report Nos. Special report additional to the Annual Greenwich observations Series,viii, HMSO, London)*. Royal Greenwich Observatory. Retrieved from https://www.ngdc.noaa.gov/stp/space-weather/online-publications/greenwich/1874-1954_greenwich-sunspot-and-geomagnetic-storm-data.pdf

Kahler, S. W., Akiyama, S., & Gopalswamy, N. (2012). Deflections of fast coronal mass ejections and the properties of associated solar energetic particle events. *The Astrophysical Journal*, *754*(2), 100. https://doi.org/10.1088/0004-637x/754/2/100

Karinen, K. A., & Mursula, K. (2005). A new reconstruction of the D_{st} index for 1932-2002. *Annales Geophysicae*, *23*(2), 475–485. https://doi.org/10.5194/angeo-23-475-2005

Kataoka, R., Miyoshi, Y., Shiokawa, K., Nishitani, N., Keika, K., Amano, T., & Seki, K. (2024). Magnetic storm-time red aurora as seen from hokkaido, Japan on 1 december 2023 associated with high-density solar wind. *Geophysical Research Letters*, *51*(12), e2024GL108778. https://doi.org/10.1029/2024GL108778

Kay, C., Gopalswamy, N., Xie, H., & Yashiro, S. (2017). Deflection and rotation of CMEs from active region 11158. *Solar Physics*, *292*(6), 78. https://doi.org/10.1007/s11207-017-1098-z

Kim, R., Cho, K., Moon, Y., Kim, Y., Yi, Y., Dryer, M., et al. (2005). Forecast evaluation of the coronal mass ejection (CME) geoeffectiveness using halo CMEs from 1997 to 2003. *Journal of Geophysical Research*, *110*(A11). https://doi.org/10.1029/2005ja011218

Knipp, D., Fraser, B., Shea, M., & Smart, D. (2018). On the little-known consequences of the 4 august 1972 ultra-fast coronal mass ejecta: Facts, commentary, and call to action. *Space Weather*, *16*(11), 1635–1643. https://doi.org/10.1029/2018SW002024

Kozyra, J. U., Nagy, A. F., & Slater, D. W. (1997). High-altitude energy source(s) for stable auroral red arcs. *Reviews of Geophysics*, *35*(2), 155–190. https://doi.org/10.1029/96RG03194

Laundal, K. M., & Richmond, A. D. (2017). Magnetic coordinate systems. *Space Science Reviews*, *206*(1–4), 27–59. https://doi.org/10.1007/s11214-016-0275-y

Lefèvre, L., Vennerstrøm, S., Dumbović, M., Vršnak, B., Sudar, D., Arlt, R., et al. (2016). Detailed analysis of solar data related to historical extreme geomagnetic storms: 1868-2010. *Solar Physics*, *291*(5), 1483–1531. https://doi.org/10.1007/s11207-016-0892-3

Liu, Y., Luhmann, J., Kajdič, P., Kilpua, E., Lugaz, N., Nitta, N., et al. (2014). Observations of an extreme storm in interplanetary space caused by successive coronal mass ejections. *Nature Communications*, *5*(1), 3481. https://doi.org/10.1038/ncomms4481

Lockwood, M. (2025). The celestial rubbish dump. *Astronomy and Geophysics*, *66*(3), 3.36–3.42. https://doi.org/10.1093/astrogeo/ataf023

Lockwood, M. (2023). Universal Time effects on substorm growth phases and onsets. *Journal of Geophysical Research: Space Physics*, *128*(11), e2023JA031671. https://doi.org/10.1029/2023JA031671

Lockwood, M., Chambodut, A., Barnard, L. A., Owens, M. J., Clarke, E., & Mendel, V. (2018). A homogeneous *aa* index: 1. Secular variation. *Journal of Space Weather and Space Climate*, *8*, A53. https://doi.org/10.1051/swsc/2018038

Lockwood, M., Chambodut, A., Finch, I. D., Barnard, L. A., Owens, M. J., & Haines, C. (2019). Time-of-day/time-of-year response functions of planetary geomagnetic indices. *Journal of Space Weather and Space Climate*, *9*, A20. https://doi.org/10.1051/swsc/2019017

Lockwood, M., & Cowley, S. W. H. (1992). Ionospheric convection and the substorm cycle. In C. Mattock (Ed.), *Substorms 1, proceedings of the first international conference on substorms, ics-1. Proceedings of First International Conference on Substorms, ICS-1,held at Kiruna, Sweden on 23-27 March 1992, ESA-SP-335* (pp. 99–109). European Apace Agency Publications.

Lockwood, M., & Cowley, S. W. H. (2022). Magnetosphere-ionosphere coupling: Implications of non-Equilibrium conditions. *Frontiers in Astronomy and Space Sciences*, *9*, 908571. https://doi.org/10.3389/fspas.2022.908571

Lockwood, M., Finch, I. D., Chambodut, A., Barnard, L. A., Owens, M. J., & Clarke, E. (2018). A homogeneous *aa* index: 2. Hemispheric asymmetries and the equinoctial variation. *Journal of Space Weather and Space Climate*, *8*, A58. https://doi.org/10.1051/swsc/2018044

Lockwood, M., & Hapgood, M. (2007). The Rough Guide to the Moon and Mars. *Astronomy and Geophysics*, *48*(6), 6.11–6.17. https://doi.org/10.1111/j.1468-4004.2007.48611.x

Lockwood, M., Owens, M. J., Barnard, L. A., Scott, C. J., Frost, A. M., Yu, B., & Chi, Y. (2022). Application of historic datasets to understanding open solar flux and the 20th-century grand solar maximum. 1. Geomagnetic, ionospheric, and sunspot observations. *Frontiers in Astronomy and Space Sciences*, *9*, 960775. https://doi.org/10.3389/fspas.2022.960775

Lockwood, M., Owens, M. J., Brown, W., & Vázquez, M. (2025). The 2024 May event in the context of auroral activity over the past 375 yr. *Monthly Notices of the Royal Astronomical Society*, *540*(4), 3596–3624. https://doi.org/10.1093/mnras/staf827

Lugaz, N., Roussev, I. I., & Sokolov, I. V. (2008). The august 24, 2002 coronal mass ejection: When a western limb event connects to earth. *Proceedings of the International Astronomical Union*, *4*(S257), 391–398. https://doi.org/10.1017/s1743921309029615

Magdalenić, J., Marqué, C., Krupar, V., Mierla, M., Zhukov, A. N., Rodriguez, L., et al. (2014). TRACKING the CME-driven shock wave on 2012 MARCH 5 and radio triangulation of associated radio emission. *The Astrophysical Journal*, *791*(2), 115. https://doi.org/10.1088/0004-637x/791/2/115

Mäkelä, P., Gopalswamy, N., Xie, H., Mohamed, A. A., Akiyama, S., & Yashiro, S. (2013). Coronal hole influence on the observed structure of interplanetary CMEs. *Solar Physics*, *284*(1), 59–75. https://doi.org/10.1007/s11207-012-0211-6

Mayaud, P.-N. (1972). The aa indices: A 100-year series characterizing the magnetic activity. *Journal of Geophysical Research*, *77*(34), 6870–6874. https://doi.org/10.1029/ja077i034p06870

Mikhalev, A. (2024). Auroras during extreme geomagnetic storms: Some features of mid-latitude aurora on February 11, 1958. *Solar-Terrestrial Physics*, 55–61. https://doi.org/10.12737/stp-102202406

Mishra, S. K., & Srivastava, A. K. (2019). Linkage of geoeffective stealth CMEs associated with the eruption of coronal plasma channel and jet-like structure. *Solar Physics*, *294*(12), 169. https://doi.org/10.1007/s11207-019-1560-1

Miyaoka, H., Hirasawa, T., Yumoto, K., & Tanaka, Y. (1990). Low latitude aurorae on October 21, 1989. I. *Proceedings of the Japan Academy, Series B*, *66*(3), 47–51. https://doi.org/10.2183/pjab.66.47

Mohamed, A. A., Gopalswamy, N., Yashiro, S., Akiyama, S., Mäkelä, P., Xie, H., & Jung, H. (2012). The relation between coronal holes and coronal mass ejections during the rise, maximum, and declining phases of Solar Cycle 23. *Journal of Geophysical Research*, *117*(A1). https://doi.org/10.1029/2011ja016589

Möstl, C., Farrugia, C. J., Kilpua, E. K. J., Jian, L. K., Liu, Y., Eastwood, J. P., et al. (2012). Multi-point shock and flux rope analysis of multiple Interplanetary Coronal Mass Ejections around 2000 August 1 in the heliosphere. *The Astrophysical Journal*, *758*(1), 10. https://doi.org/10.1088/0004-637x/758/1/10

Möstl, C., Temmer, M., Rollett, T., Farrugia, C. J., Liu, Y., Veronig, A. M., et al. (2010). STEREO and Wind observations of a fast ICME flank triggering a prolonged geomagnetic storm on 5–7 April 2010. *Geophysical Research Letters*, *37*(24). https://doi.org/10.1029/2010gl045175

Muller, C. (1990). The Carrington solar flares of 1859: Consequences on life. *Origins of Life and Evolution of the Biosphere*, *44*(3), 185–195. https://doi.org/10.1007/s11084-014-9368-3

Mursula, K., Holappa, L., & Karinen, A. (2011). Uneven weighting of stations in the Dst index. *Journal of Atmospheric and Solar-Terrestrial Physics*, *73*(2–3), 316–322. https://doi.org/10.1016/j.jastp.2010.04.007

Newell, P. T., & Gjerloev, J. W. (2011a). Evaluation of SuperMAG auroral electrojet indices as indicators of substorms and auroral power. *Journal of Geophysical Research*, *116*(A12), 2011JA016779. https://doi.org/10.1029/2011JA016779

Newell, P. T., & Gjerloev, J. W. (2011b). Substorm and magnetosphere characteristic scales inferred from the SuperMAG auroral electrojet indices. *Journal of Geophysical Research*, *116*(A12), 2011JA016936. https://doi.org/10.1029/2011JA016936

Newton, H. (1943). Solar flares and magnetic storms. *Monthly Notices of the Royal Astronomical Society*, *103*(5), 244–257. https://doi.org/10.1093/mnras/103.5.244

Nicholson, S. (1938). The great sunspot of January 1938. *Eos, Transactions American Geophysical Union*, *19*(1), 203–204. https://doi.org/10.1029/TR019i001p00203

Nitta, N., & Mulligan, T. (2017). Earth-affecting coronal mass ejections without obvious low coronal signatures. *Solar Physics*, *292*(9), 125. https://doi.org/10.1007/s11207-017-1147-7

Nitta, N., Mulligan, T., Kilpua, E., Lynch, B., Mierla, M., O'Kane, J., et al. (2021). Understanding the origins of problem geomagnetic storms associated with "stealth" coronal mass ejections. *Space Science Reviews*, *217*(8), 82. https://doi.org/10.1007/s11214-021-00857-0

Ohtani, S., Nosé, M., Rostoker, G., Singer, H., Lui, A. T. Y., & Nakamura, M. (2001). Storm-substorm relationship: Contribution of the tail current to *Dst*. *Journal of Geophysical Research*, *106*(A10), 21199–21209. https://doi.org/10.1029/2000JA000400

Owens, M. J., Barnard, L. A., Verbeke, C., McGinness, B. P. S., Turner, H., Chi, Y., et al. (2025). Implications of using spheroidal "Cone Model" CMEs in solar-wind models. *Space Weather*, *23*(6), e2025SW004397. https://doi.org/10.1029/2025sw004397

Partamies, N., Juusola, L., Tanskanen, E., & Kauristie, K. (2013). Statistical properties of substorms during different storm and solar cycle phases. *Annales Geophysicae*, *31*(2), 349–358. https://doi.org/10.5194/angeo-31-349-2013

Pulkkinen, T. (2007). Space weather: Terrestrial perspective. *Living Reviews in Solar Physics*, *4*, 1. https://doi.org/10.12942/lrsp-2007-1

Rassoul, H. K., Rohrbaugh, R. P., & Tinsley, B. A. (1992). Low-latitude particle precipitation and associated local magnetic disturbances. *Journal of Geophysical Research*, *97*(A4), 4041–4052. https://doi.org/10.1029/91JA03028

Richardson, I. G., & Cane, H. V. (2010). Near-Earth interplanetary Coronal Mass Ejections during solar cycle 23 (1996–2009): Catalog and summary of properties. *Solar Physics*, *264*(1), 189–237. https://doi.org/10.1007/s11207-010-9568-6

Richmond, A. D. (1995). Ionospheric Electrodynamics using magnetic apex coordinates. *Journal of Geomagnetism and Geoelectricity*, *47*(2), 191–212. https://doi.org/10.5636/jgg.47.191

Rodriguez, L., Zhukov, A. N., Cid, C., Cerrato, Y., Saiz, E., Cremades, H., et al. (2009). Three frontside full halo coronal mass ejections with a nontypical geomagnetic response. *Space Weather*, *7*(6), S06003. https://doi.org/10.1029/2008sw000453

Schulz, M., & Lanzerotti, L. (1974). *Particle diffusion in the radiation*. Springer. https://doi.org/10.1007/978-3-642-65675-0

Shiokawa, K., Miyoshi, Y., Brandt, P. C., Evans, D. S., Frey, H. U., Goldstein, J., & Yumoto, K. (2013). Ground and satellite observations of low-latitude red auroras at the initial phase of magnetic storms. *Journal of Geophysical Research: Space Physics*, *118*(1), 256–270. https://doi.org/10.1029/2012JA018001

Shiokawa, K., Yumoto, K., Tanaka, Y., Oguti, T., & Kiyama, Y. (1994). Low-latitude auroras observed at Moshiri and Rikubetsu (L=1.6) during magnetic storms on February 26, 27, 29, and May 10, 1992. *Journal of Geomagnetism andGeoelectricity*, *46*(3), 231–252. https://doi.org/10.5636/jgg.46.231

Temmer, M., Veronig, A. M., Peinhart, V., & Vršnak, B. (2014). Asymmetry in the CME-CME interaction process for the events from 2011 February 14–15. *The Astrophysical Journal*, *785*(2), 85. https://doi.org/10.1088/0004-637x/785/2/85

Tinsley, B. A., Rohrbaugh, R., Rassoul, H., Sahai, Y., Teixeira, N. R., & Slater, D. (1986). Low-latitude aurorae and storm time current systems. *Journal of Geophysical Research*, *91*(A10), 11257–11269. https://doi.org/10.1029/JA091iA10p11257

Tokumaru, M., Kojima, M., Fujiki, K., Yamashita, M., & Baba, D. (2005). Interplanetary consequences caused by the extremely intense solar activity during October–November 2003. *Journal of Geophysical Research*, *110*(A1), 2004JA010656. https://doi.org/10.1029/2004JA010656

UN. (2024). *Demographic yearbook 2023 (technical report no. ST/ESA/STAT/SER.R/53)*. U.N. Department of Economic and Social Affairs. Retrieved from https://desapublications.un.org/publications/demographic-yearbook-2023

Villante, U., & Regi, M. (2008). Solar flare effect preceding Halloween storm (28 October 2003): Results of a worldwide analysis. *Journal of Geophysical Research*, *113*(A3), 2008JA013132. https://doi.org/10.1029/2008JA013132

Wang, Y., Shen, C., Wang, S., & Ye, P. (2004). Deflection of coronal mass ejection in the interplanetary medium. *Solar Physics*, *222*(2), 329–343. https://doi.org/10.1023/b:sola.0000043576.21942.aa

Watari, S. (2022). Extremely large flares/multiple large flares expected from sunspot groups with large area. *Earth Planets and Space*, *74*(1), 115. https://doi.org/10.1186/s40623-022-01676-5

Wu, C., Wu, S. T., Dryer, M., Fry, C. D., Berdichevsky, D., Smith, Z., et al. (2005). Flare-generated shock evolution and geomagnetic storms during the "Halloween 2003 epoch": 29 October to 2 November. *Journal of Geophysical Research*, *110*(A9), 2005JA011011. https://doi.org/10.1029/2005JA011011

Wygant, J., Rowland, D., Singer, H. J., Temerin, M., Mozer, F., & Hudson, M. K. (1998). Experimental evidence on the role of the large spatial scale electric field in creating the ring current. *Journal of Geophysical Research*, *103*(A12), 29527–29544. https://doi.org/10.1029/98ja01436

Yardley, S. L., Pagano, P., Mackay, D. H., & Upton, L. A. (2021). Determining the source and eruption dynamics of a stealth CME using NLFFF modelling and MHD simulations. *Astronomy & Astrophysics*, *652*, A160. https://doi.org/10.1051/0004-6361/202141142

Zhang, J., Richardson, I. G., Webb, D. F., Gopalswamy, N., Huttunen, E., Kasper, J. C., & Zhukov, A. N. (2007). Solar and interplanetary sources of major geomagnetic storms (dst less than or equal to -100nt) during 1996–2006. *Journal of Geophysical Research*, *112*(A10), A10102. https://doi.org/10.1029/2007ja012321